HAL
open science

The earliest phases of high-mass star formation: a 3 square degree millimeter continuum mapping of Cygnus X

Frédérique Motte, Sylvain Bontemps, P. Schilke, N. Schneider, K. M. Menten, D. Broguière

To cite this version:

Frédérique Motte, Sylvain Bontemps, P. Schilke, N. Schneider, K. M. Menten, et al.. The earliest phases of high-mass star formation: a 3 square degree millimeter continuum mapping of Cygnus X. Astronomy and Astrophysics - A&A, 2007, 476, pp.1243-1260. 10.1051/0004-6361:20077843 . hal-00167466

HAL Id: hal-00167466

https://hal.science/hal-00167466v1

Submitted on 21 Aug 2007

HAL is a multi-disciplinary open access archive for the deposit and dissemination of scientific research documents, whether they are published or not. The documents may come from teaching and research institutions in France or abroad, or from public or private research centers.

L'archive ouverte pluridisciplinaire **HAL**, est destinée au dépôt et à la diffusion de documents scientifiques de niveau recherche, publiés ou non, émanant des établissements d'enseignement et de recherche français ou étrangers, des laboratoires publics ou privés.

Astronomy & Astrophysics manuscript no. 7843.hyper32379
August 21, 2007
© ESO 2007

hal-00167466, version 1 - 21 Aug 2007

The earliest phases of high-mass star formation: a 3 square degree millimeter continuum mapping of Cygnus X⋆

F. Motte[1,2], S. Bontemps[3], P. Schilke[4], N. Schneider[1,5], K. M. Menten[4], and D. Broguière[6]

[1] Laboratoire AIM, CEA/DSM - CNRS - Université Paris Diderot, DAPNIA/Service d'Astrophysique, Bât. 709, CEA-Saclay, F-91191 Gif-sur-Yvette Cédex, France
e-mail: motte@cea.fr
[2] California Institute of Technology, Downs Laboratory of Physics, Mail Stop 320-47, 1200 E California Blvd, Pasadena, CA 91125, USA
[3] OASU/LAB-UMR 5804, CNRS - Université Bordeaux 1, 2 rue de l'Observatoire, BP 89, 33270 Floirac, France
[4] Max-Planck-Institut für Radioastronomie, Auf dem Hügel 69, 53121 Bonn, Germany
[5] I. Physik. Institut, Universität Köln, 50937 Köln, Germany
[6] IRAM, 300 rue de la Piscine, F-38406 St. Martin d'Hères, France

Received 10 May 2007/ Accepted 23 July 2007

ABSTRACT

Aims. Our current knowledge of high-mass star formation is mainly based on follow-up studies of bright sources found by *IRAS*, and is thus biased against its earliest phases, inconspicuous at infrared wavelengths. We therefore started searching, in an unbiased way and in the closest high-mass star-forming complexes, for the high-mass analogs of low-mass pre-stellar cores and class 0 protostars.
Methods. We have made an extensive 1.2 mm continuum mosaicing study of the Cygnus X molecular cloud complex using the MAMBO cameras at the IRAM 30 m telescope. The $\sim 3^{\circ 2}$ imaged areas cover all the high-column density ($A_V \geq 15$ mag) clouds of this nearby ($\sim$ 1.7 kpc) cloud complex actively forming OB stars. We then compared our millimeter maps with mid-infrared images, and have made SiO(2-1) follow-up observations of the best candidate progenitors of high-mass stars.
Results. Our complete study of Cygnus X with $\sim$ 0.09 pc resolution provides, for the first time, an unbiased census of massive young stellar objects. We discover 129 massive dense cores (*FWHM* size $\sim$ 0.1 pc, $M_{1.2\,\mathrm{mm}} = 4 - 950\ M_\odot$, volume-averaged density $\sim 10^5$ cm^{-3}), among which $\sim$ 42 are probable precursors of high-mass stars. A large fraction of the Cygnus X dense cores (2/3 of the sample) remain undetected by the *MSX* satellite, regardless of the mass range considered. Among the most massive ($> 40\ M_\odot$) cores, infrared-quiet objects are driving powerful outflows traced by SiO emission. Our study qualifies 17 cores as good candidates for hosting massive infrared-quiet protostars, while up to 25 cores potentially host high-luminosity infrared protostars. We fail to discover in the high-mass analogs of pre-stellar dense cores ($\sim$ 0.1 pc, $> 10^4$ cm^{-3}) in Cygnus X, but find several massive starless clumps ($\sim$ 0.8 pc, 7×10^3 cm^{-3}) that might be gravitationally bound.
Conclusions. Since our sample is derived from a single molecular complex and covers every embedded phase of high-mass star formation, it gives the first statistical estimates of their lifetime. In contrast to what is found for low-mass class 0 and class I phases, the infrared-quiet protostellar phase of high-mass stars may last as long as their better-known high-luminosity infrared phase. The statistical lifetimes of high-mass protostars and pre-stellar cores ($\sim 3 \times 10^4$ yr and $< 10^3$ yr) in Cygnus X are one and two order(s) of magnitude smaller, respectively, than what is found in nearby, low-mass star-forming regions. We therefore propose that high-mass pre-stellar and protostellar cores are in a highly dynamic state, as expected in a molecular cloud where turbulent processes dominate.

Key words. dust — H II regions — ISM: individual (Cygnus X) — ISM: structure — stars: formation — submillimeter

1. Introduction

High-mass (OB, $> 8\ M_\odot$) stars, though few in number, play a major role in the energy budget of galaxies. Our current understanding of their formation, however, remains very schematic, especially concerning the earliest phases of the process. High-mass stars are known to form in dense cores within molecular cloud complexes, by accretion (Yorke & Sonnhalter 2002; Krumholz et al. 2007) and/or coalescence (e.g. Bonnell et al. 2001). The copious UV flux emitted by a newly-formed central star heats and ionizes its parental molecular cloud, leading to the formation and development of a hot core (e.g. Helmich & van Dishoek 1997) and afterwards an H II region (see a review by Churchwell 1999).

In the past few years, the progenitors of ultracompact H II (UCH II) regions (sources that have not yet begun to ionize their environment in a detectable way) have been searched among *IRAS* point sources. The criteria generally used aim at selecting high-luminosity ($> 10^3\ L_\odot$) stellar embryos embedded in a massive envelope and associated with hot gas but no UCH II region (see Kurtz et al. 2000). In fact, most surveys focussed on red *IRAS* sources with colors satisfying the Wood & Churchwell (1989) criteria (originally set for selecting UCH II regions) but not detected in radio centimeter surveys. The presence of an envelope around the *IRAS* sources is confirmed by their association with high-density gas, and the existence of hot

Send offprint requests to: F. Motte

⋆ Tables 1–2, Figs. 12–15, and Appendices A and B are only available in electronic form at http://www.aanda.org. Fits images associated with Figs. 2a–c and catalogs built from Tables 1–2 can be queried from the CDS via anonymous ftp to cdsarc.u-strasbg.fr (130.79.128.5) or via http://cdsweb.u-strasbg.fr/cgi-bin/qcat?J/A+A/.

gas by the detection of a hot core and water or methanol masers (e.g. Bronfman et al. 1996; Plume et al. 1997). In this way, studies by e.g., Molinari et al. (2000) and Sridharan et al. (2002) have identified massive young stellar objects harboring high-luminosity infrared protostars (see also Mueller et al. 2002; Faúndez et al. 2004).

Such surveys are biased against younger and, thus probably colder, massive young stellar objects which could be inconspicuous in the mid-infrared bands of *IRAS* and the *Midcourse Space Experiment* (*MSX*). These high-mass analogs of low–mass class 0 protostars and pre-stellar cores (cf. André et al. 2000) should be best detected via far-infrared to (sub)millimeter dust continuum and high-density molecular line tracers. Serendipitous discoveries of a few infrared-quiet massive young stellar objects have been made in submillimeter continuum maps (e.g. Molinari et al. 1998; Motte et al. 2003; Sandell & Sievers 2004; Hill et al. 2005) and as absorption regions in mid-infrared images (often called "infrared dark clouds", e.g. Carey et al. 2000; Thompson et al. 2005; Rathborne et al. 2006). These studies suggest that, in the high-mass star formation process also, infrared-quiet phases must exist and be associated with significant populations of young protostars and/or pre-stellar cores. The lack of statistics, homogeneity, and angular resolution of studies such as the above, however, prevents the determination of the basic characteristics of these infrared-quiet objects.

To make significant progress, one needs to search in a systematic way for the earliest phases of high-mass star formation in nearby complexes. One of the most appropriate methods is to survey entire molecular cloud complexes in which high-mass stars are forming, using tracers of high-density clouds and protostellar activity signatures. We therefore started a multitracer study of Cygnus X, which is one of the richest molecular and H II complexes located at less than 3 kpc from the Sun. The molecular cloud complex is massive (4×10^6 $M_\odot$) and extends over $\sim$ 100 pc in diameter (cf. Leung & Thaddeus 1992). Found to be part of the local spiral arm, this complex has been located at 1.7 kpc from the Sun by the recent ^{13}CO study of Schneider et al. (2006). Cygnus X has a rich collection of H II regions (see centimeter free-free emission maps by Wendker et al. 1991, and infrared images from *MSX* presented in Figs. 7–9 of Schneider et al. 2006), indicating recent high-mass star formation. It is associated with several OB associations (see Uyaniker et al. 2001 and references therein), amongst them one of the largest in our Galaxy (Cyg OB2, cf. Knödlseder 2000). It also contains several well-known massive young stellar objects like DR21, DR21(OH), AFGL 2591, S106-IR, and W75N (e.g. Smith et al. 1998; van der Tak et al. 1999; Schneider et al. 2002; Shepherd et al. 2004). Small parts of the Cygnus X cloud complex have already been observed in (sub)millimeter continuum emission (e.g. Chandler et al. 1993a; Richer et al. 1993; Vallée & Fiege 2006; Davis et al. 2007).

The present paper tackles the following key questions: do high-mass pre-stellar cores exist? What are the lifetimes of high-mass pre-stellar cores, infrared-quiet protostars, and high-luminosity infrared protostars? What are the main physical processes leading from pre-stellar objects to high-mass protostars? We report an extensive 1.2 mm continuum study of the Cygnus X complex complemented by SiO(2-1) follow-up observations of the best candidate progenitors of high-mass stars. From the MAMBO-2 imaging ($\sim 3^{\circ 2}$) of the entire complex presented in Sect. 2, we make a complete census of the compact cloud fragments and larger-scale structures (Sect. 3). We determine the main characteristics of these new millimeter sources in Sect. 3, and search for signposts of protostellar activity including SiO emission (a tracer of outflow activity) in Sect. 4. Section 5 identifies 129 massive dense cores, among which 42 are probable precursors of high-mass stars. This unbiased sample of young embedded massive stars reveals 17 dense cores that are excellent candidates for harboring high-mass protostars in their infrared-quiet phase. The present paper also gives the first statistical results on the lifetime of high-mass protostars and pre-stellar cores. Finally, Sect. 6 summarizes our conclusions, and Appendices A and B describe our data reduction and source extraction techniques.

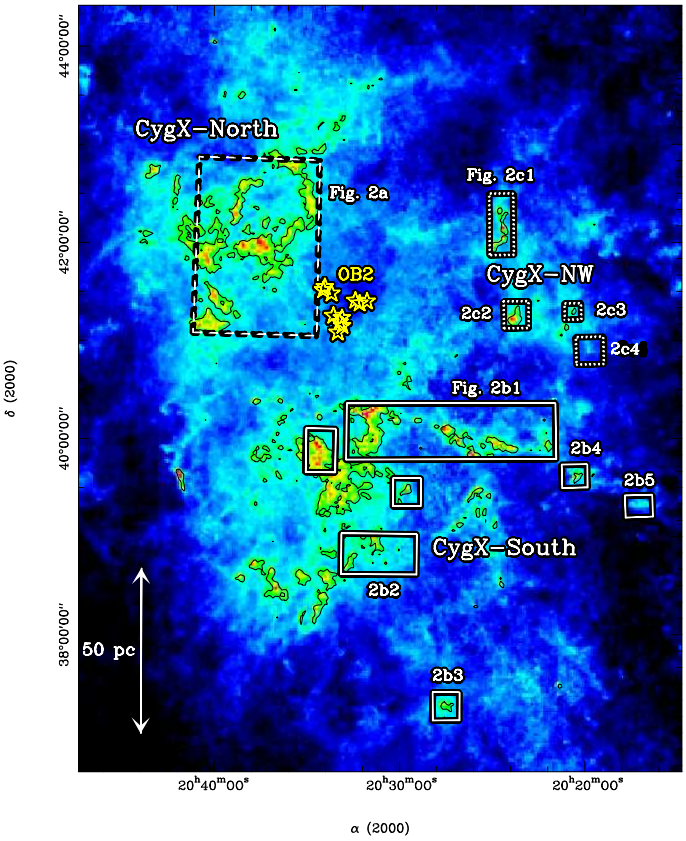

Fig. 1. Extinction map of the Cygnus X complex derived by Bontemps et al. (in prep.) from the stellar reddening of background stars in JHK, using the 2MASS database and a pixel size of 1.3′. The high-extinction regions are yellow and outlined by the 15 mag contour level. The three molecular cloud ensembles identified by Schneider et al. (2006) are labeled and the nearby Cygnus OB2 association is indicated. The fields mapped with MAMBO or MAMBO-2 are schematically outlined and add up to $\sim 3^{\circ 2}$.

2. Observations and data reduction

2.1. Imaging the entire molecular complex

The Cygnus X molecular cloud complex covers up to $\sim 30^{\circ 2}$ (see Fig. 1 of Schneider et al. 2006) but the sites of high-mass star formation are found in its highest-density parts. We therefore used an infrared extinction map produced from 2MASS[1] data (cf. Fig. 1 and Bontemps et al. in prep.) to select the high-column density ($A_V \geq 15$ mag) clouds of Cygnus X

[1] The Two Micron All Sky Survey was performed by the University of Massachussets and IPAC/Caltech and funded by NASA and NSF.

to be mapped in millimeter continuum emission. Figure 1 and Schneider et al. (2006) show that the Cygnus X molecular complex contains several ensembles of dense molecular clouds which extend over $\sim$ 50 parsecs. In the following, we use the name "CygX-North" for the north-eastern group of clouds which harbors the well-known sources DR21 and W75N, "CygX-South" for the southern region containing AFGL 2591 and S106-IR, and "CygX-NW" for the north-western filamentary clouds. The mappings necessary to cover the high-column density clouds of Cygnus X are outlined in Fig. 1 and cover a total area of $\sim 3^{\circ 2}$.

2.2. Dust continuum observations at 1.2 mm

The Cygnus X molecular complex was imaged at 1.2 mm with the MPIfR bolometer arrays installed at the IRAM[2] 30 m telescope at Pico Veleta (Spain). The passband of the MPIfR bolometers has an equivalent width of $\approx$ 70 GHz and is centered at $\nu_{\rm eff} \approx 240$ GHz (Kreysa et al. 1998). The MAMBO (37 channels) camera was used in February-April 1999, January-March 2000, and December 2000-May 2001 for a total integration time of $\sim$ 30 hours. The MAMBO-2 (117 channels) camera was used for $\sim$ 33 hours as part of the observing pools organized by IRAM between November 2002 and March 2003. A total of 142 large on-the-fly maps were taken using a fast-mapping technique similar to that described by Teyssier & Sievers (1998). These maps consist of a series of rows scanned in azimuth with a velocity of 8″/sec and spaced by 22″ (respectively 46″) steps in elevation when using MAMBO or MAMBO-2. The typical azimuthal size of individual maps is $\sim$ 7.5′ with MAMBO versus $\sim$ 11′ with MAMBO-2. The signal of each bolometer is modulated by the secondary mirror which is wobbling with a frequency of 2 Hz and a throw in azimuth of 70″. The resulting dual-beam maps were reduced with the IRAM software for bolometer-array data (NIC; cf. Broguière et al. 1995) using the EKH restoration algorithm (Emerson et al. 1979) and a skynoise reduction technique developed by us (see Appendix A). The imaging of each requested field was obtained by combining partially overlapping restored on-the-fly maps.

The main beam was measured and found to have a *HPBW* size of $\sim$ 11″ using Uranus and Mars. The absolute pointing of the telescope was found to be accurate to within $\sim$ 5″. The data were all taken in winter but with heterogeneous weather conditions. The zenith atmospheric optical depth varied between 0.1 and 0.5 and the skynoise level was low to high (correlation factor from 0.2 to 1). The resulting rms noise in individual maps is $\sigma = 10 - 150$ mJy beam^{-1}, reduced to $\sigma \sim 20$ mJy beam^{-1} after reduction of the skynoise (see Appendix A). The final mosaics all have $\sigma < 20$ mJy beam^{-1} rms with a median rms of $\sigma \sim 15$ mJy beam^{-1}. Uranus and Mars were also used for flux calibration and the overall absolute calibration uncertainty is estimated to be $\sim$ 20%.

2.3. SiO(2-1) observations

Pointed observations in the SiO v=0 J=2→1 transition were performed for 40 millimeter continuum sources listed in Table 1 in September 2003 and July 2004 with the IRAM 30 m telescope. We used the A100 (B100) SIS receiver and the VESPA autocorrelator with a frequency resolution of 40 kHz that is equivalent to 0.135 km s^{-1} at 86.847 GHz. The system temperature for both observing runs was between 110 and 130 K and the average rms for each data set is 0.03 K on a main beam brightness temperature scale, taking an efficiency $\eta_{\rm MB}$ of 0.78. The angular resolution of the telescope at 87 GHz is 29″. All observations were performed in position-switching mode with off-positions a few arcminutes away in azimuth. Pointing was checked regularly and was accurate to within 3″. Standard calibration sources were observed regularly and were consistent within 10%. The data were reduced with the IRAM software for spectral lines (CLASS), applying first order baselines and averaging individual spectra with rms weighting.

3. Analysis of the 1.2 mm mapping of Cygnus X

3.1. Dust continuum images

The 1.2 mm continuum images are presented in Figs. 2a-c with zooms in the left-hand parts of Figs. 3–4 (see also Figs. 12–14 which are only available electronically). The dense molecular gas sometimes follows filamentary structures (well observed in the ^{13}CO(1-0) images of Schneider et al. in prep.) and displays many compact ($\sim$ 0.1 pc) fragments. We make a complete census of these 1.2 mm fragments in Sect. 3.2 and a similar but less complete census of larger-scale ($\sim$ 1 pc) cloud structures in Sect. 3.3.

The MAMBO-2 mosaics are sensitive to spatial scales ranging from $\sim$ 0.09 pc (corresponding to an *HPBW* of 11″ at 1.7 kpc) to $\sim$ 5 pc (i.e. the mean azimuth extent of individual maps $\sim$ 10′ at 1.7 kpc). The resulting spatial dynamic is $\sim$ 55, larger than that of other (sub)millimeter dust continuum observations made with SCUBA at the JCMT, SIMBA at the SEST, or BOLOCAM at the CSO. Therefore, large fast-mapping images with MAMBO-2 are currently the best tool to study the density structure of molecular clouds with high spatial resolution. Given the dynamic range in the MAMBO-2 image (within a 11″ beam, cold dust emission ranges from $\sigma \sim 15$ mJy beam^{-1} to 6 300 mJy beam^{-1}), the Cygnus X complex is probed from $N_{\rm H_2} \sim 9 \times 10^{21}$ cm^{-2} to 2×10^{24} cm^{-2}, or similarly from $A_{\rm V} \sim 10$ mag to 2100 mag (i.e. with a column density dynamic of more than 200). The above estimate uses Eq. 1 from Motte et al. (1998) with dust temperatures of 20 K and dust opacities of $\kappa_{1.2\,\rm mm} = 0.005$ and 0.01 cm^2 g^{-1} for the lower and higher density cloud structures, respectively.

Due to the spatial filtering of cloud structures larger than clumps (i.e. > 5 pc, see Appendix A) in MAMBO-2 images, the total mass detected in millimeter continuum emission is 10 to 20 times smaller (37×10^3 $M_\odot$ in CygX-North and 26×10^3 $M_\odot$ in CygX-South) than that measured in the CO survey of Schneider et al. (2006).

3.2. Census of compact cloud fragments in Cygnus X

Since our main goal is to investigate the best potential sites of high-mass star formation, we first focus on the small-scale cloud fragments observed in our MAMBO-2 images. As expected, larger-scale ($\sim$ 1 pc) cloud structures generally have a moderate volume-averaged density ($\sim 5 \times 10^3$ cm^{-3} for a 1.2 mm peak flux of $5\sigma = 75$ mJy beam^{-1} over a diameter of 1 pc, when a 20 K dust temperature and a $\kappa_{1.2\,\rm mm} = 0.01$ cm^2 g^{-1} dust mass opacity are assumed, cf. Eqs. 1 and 2) and will therefore be less likely to form high-mass stars in the near future. We apply the source extraction technique developed by Motte et al. (2003) which uses a multi-resolution analysis (Starck & Murtagh 2006) and the Gaussclumps program

[2] IRAM is supported by INSU/CNRS (France), MPG (Germany) and IGN (Spain).

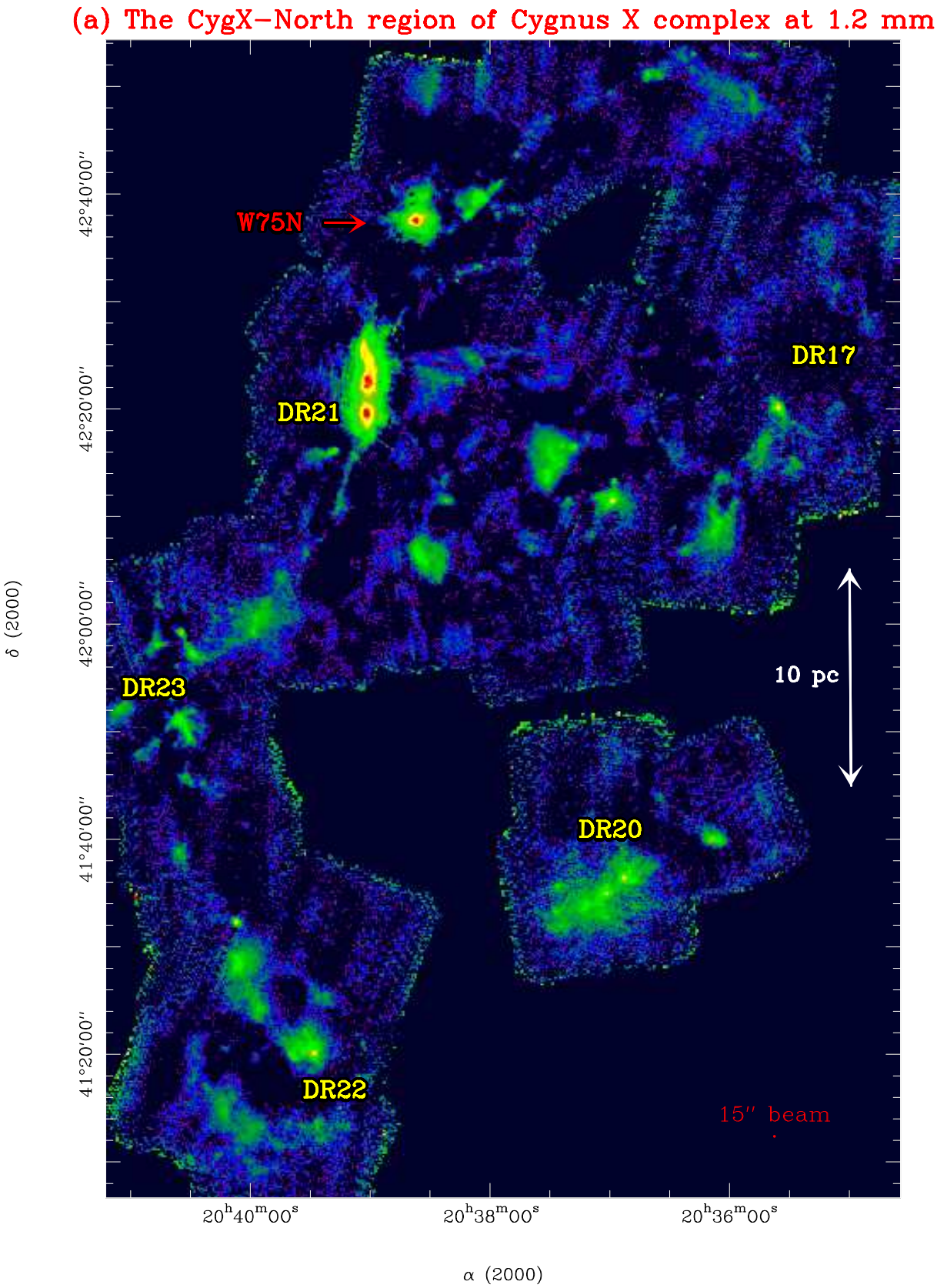

Fig. 2. Millimeter continuum imaging of the Cygnus X molecular cloud complex obtained with the MAMBO and MAMBO-2 cameras installed at the IRAM 30 m telescope. These 1.2 mm maps have been smoothed to an effective angular resolution of 15″, allowing a sensitivity of 0.1–5 pc cloud structures. The main radio sources (Downes & Rinehart 1966) and a few well-known sources are indicated as reference marks. **a** The CygX-North region (see Fig. 1 for its location): maximum flux is ∼ 8 500 mJy beam^{-1} (color scale is saturated beyond 500 mJy beam^{-1}) and rms noise level is σ = 10 – 20 mJy beam^{-1}.

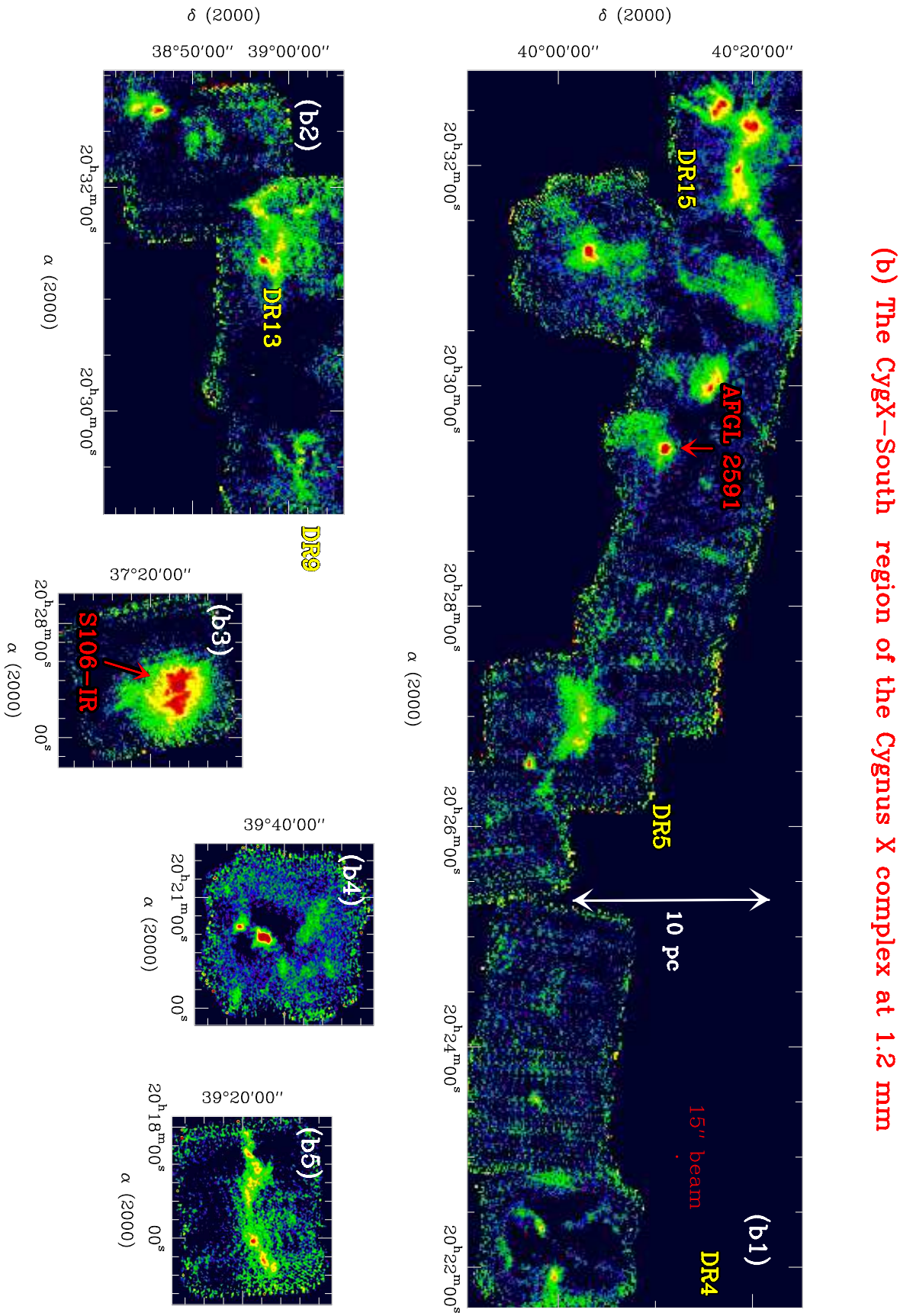

Fig. 2. (continued) **b** The CygX-South region: maximum flux is ~ 8 500 mJy beam^{-1} (color scale is saturated beyond 500 mJy beam^{-1}) and rms noise levels are 9 – 18 mJy beam^{-1} in **b1**, ~ 14 mJy beam^{-1} in **b2**, ~ 14 mJy beam^{-1} in **b3**, ~ 13 mJy beam^{-1} in **b4**, and ~ 15 mJy beam^{-1} in **b5**. Note that the MAMBO-2 maps associated with DR12 and DR6 in Fig. 1 are ignored since they do not display any compact and dense gas.

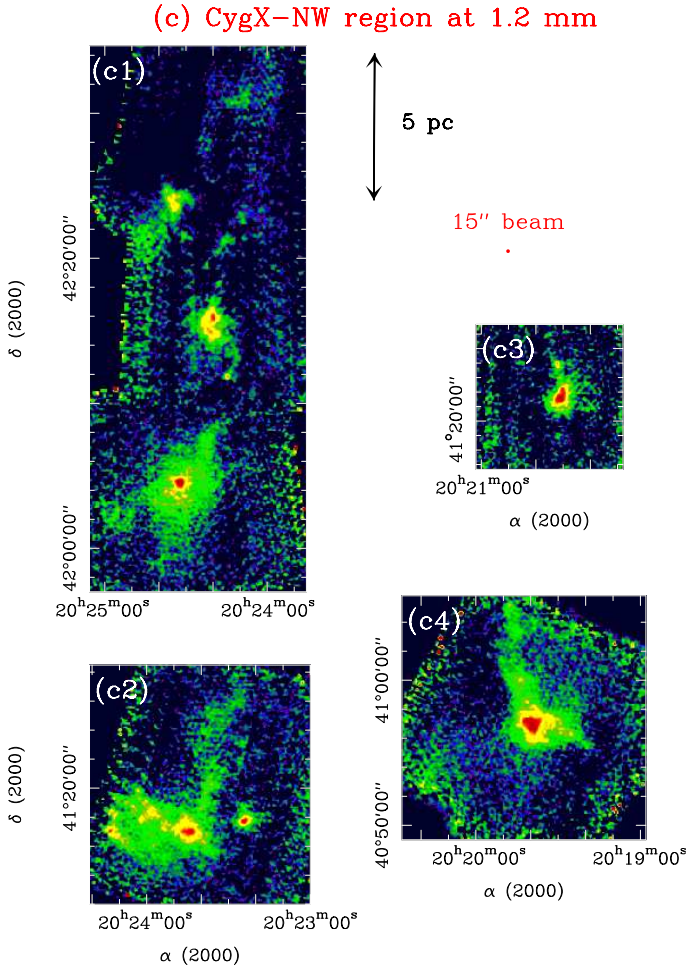

Fig. 2. (continued) **c** The CygX-NW region: maximum flux is ∼ 800 mJy beam^{-1} (color scale is saturated beyond 500 mJy beam^{-1}) and rms noise levels are 9 − 16 mJy beam^{-1} in **c1**, ∼ 13 mJy beam^{-1} in **c2**, ∼ 18 mJy beam^{-1} in **c3**, and ∼ 12 mJy beam^{-1} in **c4**.

(Stutzki & Güsten 1990; Kramer et al. 1998). We first identify 129 compact (< 1 pc) cloud fragments above the median 5σ = 75 mJy beam^{-1} level in the MAMBO-2 maps, where spatial scales larger than 1 pc have been filtered out (see e.g. Fig. 11b). We then precisely derive the 1.2 mm characteristics of each fragment by fitting a 2D-Gaussian in the image where its local background (or surrounding large-scale emission) has been entirely removed (see Appendix B for more details).

The compact fragments extracted here are marked and labeled in the left-hand parts of Figs. 3–4 and Figs. 12–14. Table 1, which is only available electronically, lists the 129 fragments discovered in Cygnus X and gives their 1.2 mm basic characteristics as estimated above. The fragments are listed in increasing RA coordinate for each region. They are numbered (Col. 1) and named after their 2000 equatorial coordinates (Col. 2). Their 1.2 mm peak flux density (Col. 3), their *FWHM* size (Col. 4), and integrated flux (Col. 5) are measured assuming a Gaussian shape. In Col. 9, we list previous names given to strong millimeter peaks of the DR21 filament (cf. Chandler et al. 1993a), as well as the name of nearby benchmark sources (e.g. Carey et al. 2000).

3.3. Large-scale cloud structures in Cygnus X

To complement the study performed in Sect. 3.2, we here make a census of the large-scale (∼ 1 pc) cloud structures of Cygnus X. We first smooth the MAMBO-2 maps to a 55″ resolution, which roughly corresponds to ∼ 0.5 pc and is the resolution of a N_2H^+ survey performed at the FCRAO (Schneider et al. in prep.). We then identify 40 large-scale cloud fragments above the median 5σ = 75 mJy beam^{-1} level and fit them by a 2-D Gaussian. Note that the skynoise reduction technique we applied may have filtered out part of the large-scale emission (for more details see Appendix A). The present analysis is therefore less secure than that performed in Sect. 3.2 for the small-scale fragments of the Cygnus X molecular clouds. Table 2, which is only available electronically, lists the 40 large-scale clumps found in Cygnus X and gives their 1.2 mm basic characteristics (in Cols. 1-6) with the same convention as in Table 1. In addition, Col. 7 lists the compact fragments (if any) harbored by each larger-scale structure.

3.4. Mass and density derived from millimeter continuum maps

The mass and density of the compact cloud fragments (< 1 pc) and large-scale structures (∼ 1 pc) of Cygnus X are determined from their dust continuum parameters given in Tables 1 and 2. These tables list the mass (Col. 6 vs 5) and volume-averaged density (Col. 7 vs 6) estimated for each identified dense core and clump using methods and assumptions described below.

Before we estimate the mass of each cloud fragment, we should ensure that the millimeter sources identifed in Sects. 3.2 and 3.3 are indeed density structures. According to previous studies of high-mass star forming regions (see e.g. Motte et al. 2003), the main source of contamination of 1.2 mm fluxes is the free-free emission from H II regions. Unfortunately, the published centimeter wavelength free-free images of Cygnus X (e.g. Wendker et al. 1991) lack the necessary angular resolution to estimate the amount of likely contamination of each 1.2 mm source. Furthermore, the spectral index of the free-free emission is unknown, precluding the extrapolation of its flux at 1.2 mm. Observations with high-density tracers such as molecular lines at the IRAM 30 m, Effelsberg, and FCRAO telescopes, as well as 350 μm continuum with SHARC II at the CSO, suggest that the vast majority of the 1.2 mm compact and larger-scale fragments are definitive density structures traced by dust emission rather than free-free centimeter sources (e.g. Schneider et al. in prep.). Fifteen millimeter sources of Table 1 are suspected to contain H II regions (cf. Sect. 5.2.1); their associated masses and densities are therefore upper limits.

We believe that the millimeter continuum emission of cloud fragments identified in Sects. 3.2 and 3.3 is mainly thermal dust emission, which is largely optically thin. For any given dust properties and gas-to-dust ratio, the 1.2 mm fluxes are thus directly related to the total (gas + dust) mass of the fragments. For present mass estimates, we use the 1.2 mm integrated fluxes ($S^{\rm int}_{1.2\,\rm mm}$) of Tables 1–2 without correction for any free-free contamination, and derive the mass ($M_{1.2\,\rm mm}$, given in Tables 1–2), as follows:

$$M_{1.2\,\rm mm} = \frac{S^{\rm int}_{1.2\,\rm mm}\, d^2}{\kappa_{1.2\,\rm mm}\, B_{1.2\,\rm mm}(T_{\rm dust})} \simeq 5.3\, M_\odot \times \left(\frac{S^{\rm int}_{1.2\,\rm mm}}{100\ \rm mJy}\right)\left(\frac{d}{1.7\ \rm kpc}\right)^2$$

$$\times\left(\frac{\kappa_{1.2\,\mathrm{mm}}}{0.01\,\mathrm{cm^2\,g^{-1}}}\right)^{-1}\left(\frac{T_{\mathrm{dust}}}{20\,\mathrm{K}}\right)^{-1}, \quad (1)$$

where $\kappa_{1.2\,\mathrm{mm}}$ is the dust opacity per unit mass column density at 1.2 mm, $B_{1.2\,\mathrm{mm}}(T_{\mathrm{dust}})$ is the Planck function for a dust temperature T_{dust}, and where we assume a distance of 1.7 kpc.

The dust mass opacity (including dust properties and gas-to-dust mass ratio) is likely to vary with density, temperature, and the evolutionary state of the emitting medium (Henning et al. 1995). Models of dust in low-mass protostellar cores (e.g. Ossenkopf & Henning 1994) suggest that a value of $\kappa_{1.2\,\mathrm{mm}} = 0.01\ \mathrm{cm^2\,g^{-1}}$ is well suited for cool (10 – 30 K) and high-density ($n_{\mathrm{H_2}} \sim 10^5\ \mathrm{cm^{-3}}$) cloud fragments. This value agrees with the cross-comparisons of dust emission surrounding an UCH II region with its CO ice absorption and gas emission (van der Tak 2002). We therefore choose a dust opacity per unit (gas + dust) mass column density of $\kappa_{1.2\,\mathrm{mm}} = 0.01\ \mathrm{cm^2\,g^{-1}}$ for compact cloud fragments. We use this value for all the dense fragments because the average dust properties of these ∼ 0.1 pc structures should not change drastically when they contain a massive protostar. We also adopt $\kappa_{1.2\,\mathrm{mm}} = 0.01\ \mathrm{cm^2\,g^{-1}}$ for larger-scale (∼ 1 pc) clumps, despite the fact that a lower value is generally used for lower-density starless cloud fragments (e.g. Ward-Thompson et al. 1999). We estimate that the absolute value taken for the dust mass opacity is uncertain by a factor of 2.

The temperature to be used in Eq. (1) is the mass-weighted dust temperature of the cloud fragments, whose value could be determined from gray-body fitting of their spectral energy distributions. Such measures are not yet available but we recently measured the ammonia rotational temperatures of the Cygnus X dense cores (Wyrowski et al. in prep.). The ratios of NH_3 (1,1) and (2,2) transitions observed with the Effelsberg 100 m telescope (40″ beam) give cold temperatures (∼ 15 K) for the material located within a 0.33 pc diameter of a millimeter peak. To estimate the temperature averaged on ∼ 0.1 pc scales, we assume a classical $\rho(r) \propto r^{-2}$ density law and inner heating ($T(r) \propto r^{-0.4}$), in agreement with small-scale fragments being highly centrally condensed and generally protostellar (cf. Sects. 5.1–5.2). We thus estimate that ∼ 0.1 pc fragments should have mass-weighted dust temperatures in the range of 15–25 K. This does not preclude any hotter or colder components from being embedded in the ∼ 0.1 pc fragments; temperature gradients will be discussed in companion papers (Schneider et al. in prep.; Wyrowski et al. in prep.). For simplicity, we assume $T_{\mathrm{dust}} = 20$ K in Eq. (1) for all the cloud fragments of Table 1. We add estimates made with $T_{\mathrm{dust}} = 40$ K for H II regions (identified in Sect. 5.2.1) and the brightest ($L_{\mathrm{bol}} > 5 \times 10^3 L_\odot$) infrared protostars of Cygnus X: IRAS 20343+4129, studied by Beuther et al. (2002) which corresponds to CygX-N5, and LkHA 225S which coincides with CygX-NW5. To avoid biasing our statistical results, we hereafter use the estimates made with a homogeneous 20 K temperature. The dust temperature of large-scale clumps is more difficult to constrain since it may vary according to the presence or absence of strong external heating. We estimate that the mass-weighted dust temperature may vary from $T_{\mathrm{dust}} = 10$ K to 20 K, and choose $T_{\mathrm{dust}} = 15$ K as an averaged value to use in Eq. (1) for the large-scale (∼ 1 pc) clumps of Table 2.

The mass estimates in Tables 1–2 are globally uncertain by a factor of 2 due to uncertain dust emissivity. The individual masses can vary by ±30% relative to each other when dust temperatures vary from 15 to 25 K, or by ±50% for the 10 to 20 K temperature range (see also Eq. 1).

The volume-averaged densities listed in Tables 1–2 and used in Tables 4–5 are estimated as follows:

$$< n_{\mathrm{H_2}} > = \frac{M_{1.2\,\mathrm{mm}}}{\frac{4}{3}\,\pi \times FWHM^3}, \quad (2)$$

where $M_{1.2\,\mathrm{mm}}$ is the mass derived by Eq. (1) and *FWHM* is the full width at half maximum, determined by Gaussian fits. Using a radius equal to one *FWHM* in Eq. (2) allows one to accurately determine the volume-averaged density because the flux (and thus the mass) measured within such an aperture corresponds to > 98% of the integrated flux (respectively total mass) of Gaussian cloud structures. The often-used, beam-averaged peak density would of course be higher, but is less relevant when estimating physical constraints such as the free-fall time.

4. Signpost of stellar activity toward the Cygnus X cloud fragments

We investigate the spatial coincidence of the compact cloud fragments identified in Sect. 3.2 with mid-infrared, SiO, centimeter free-free, and maser emission (see Sects. 4.1–4.3). Large-scale cloud structures identified in Sect. 3.3, which are associated with neither compact fragments displaying signposts of stellar activity nor bright mid-infrared sources, qualify as starless clumps as indicated in Col. 7 of Table 2.

4.1. Coincidence with mid-infrared point sources

When searching for the signature of embedded stellar embryos, the cross-correlation of compact millimeter sources with infrared catalogs is crucial. Among the near- to mid-infrared surveys that are currently available and complete for the Cygnus X complex, we choose that performed by the *MSX*[3] satellite; its angular resolution (20″) is far better than that provided by *IRAS* and its wavebands (from 8 to 21 μm) are better suited than those of 2MASS. The *Spitzer* satellite provides better angular resolution and sensitivity but the mapping of Cygnus X with the *Spitzer*/MIPS camera is far from being complete, and published results from the *Spitzer*/IRAC camera generally do not cross-correlate well with (sub)millimeter sources (see Davis et al. 2007 and the counterexample ERO1/CygX-N57 of Marston et al. 2004).

To search for coincidence with mid-infrared point sources, we carefully examine the structure of the *MSX* emission at the exact location of each compact millimeter source (see right-hand side of Figs. 3–4 and Figs. 12–14). A millimeter source is defined to be detected by *MSX* if it coincides with pointlike emission at both 8 and 21 μm. Slightly more extended *MSX* emission is considered for three developed H II regions (cf. Sect. 5.2.1): DR21 (associated with CygX-N46 and N47), S106-IR (associated with CygX-S18, S19 and S20) and IRAS 20306+4005 (associated with CygX-S39 and S40). Given the resolution of *MSX* images, *MSX* point sources have similar sizes to those of compact cloud fragments detected by MAMBO-2. The detection, at both 8 and 21 μm, allows the rejection of peaks of infrared emission created by small grains at the interface of photo-dissociation regions and molecular clumps (e.g. Abergel et al. 2002). The latter are actually externally heated sources whose peaks shift with wavelength and sometimes disappear at 21 μm. We add four more sources which are only detected at 21 μm: CygX-N30 (W75N(B)), CygX-N46 (DR21) and N47 (DR21-D), whose

[3] The *Midcourse Space Experiment* provides images observed at 8, 12, 15, and 21 μm with a 20″ resolution (Egan et al. 2001).

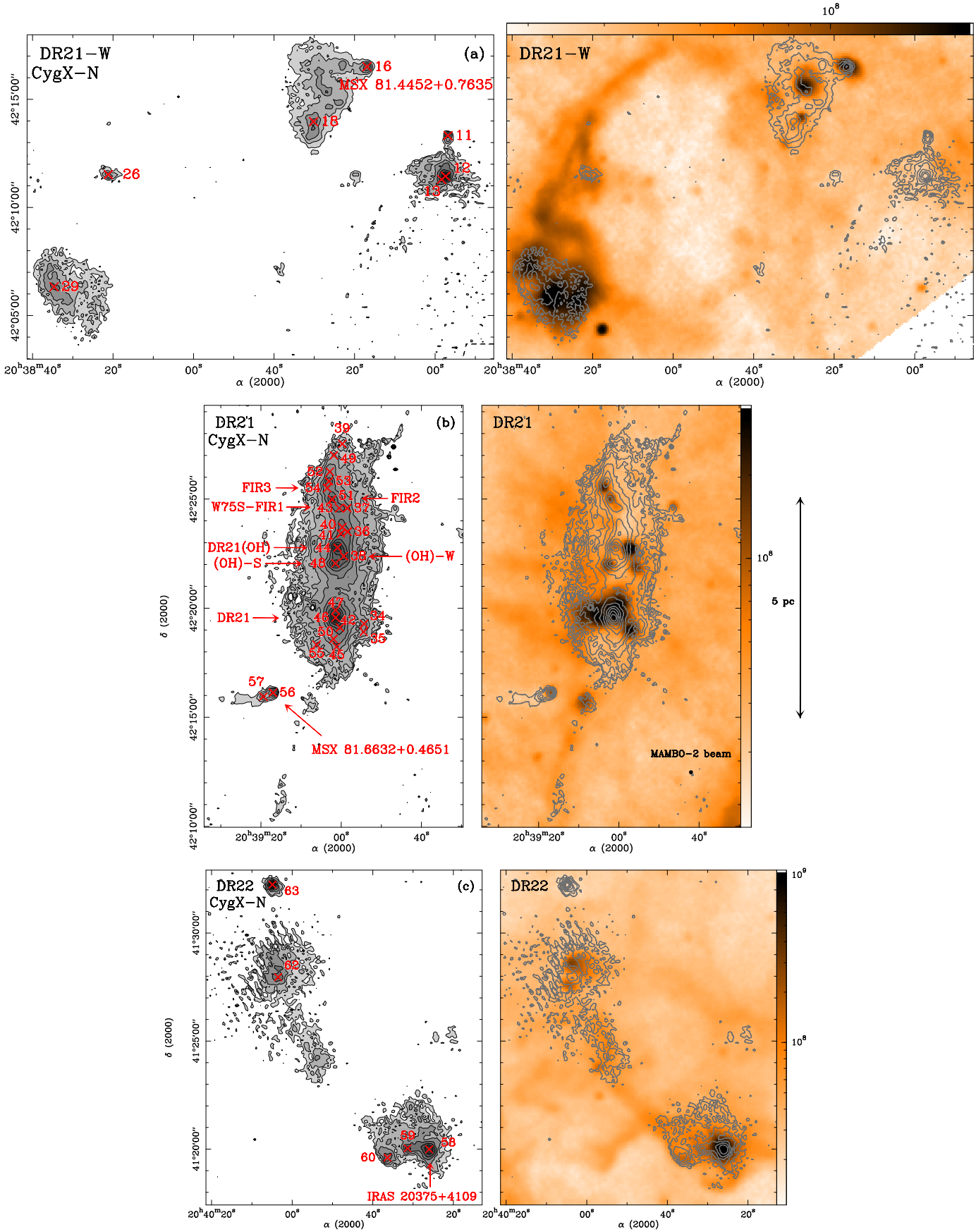

Fig. 3. MAMBO maps of CygX-North (**left**: gray-scale and contours, **right**: contours overlaid on 8 μm images obtained by *MSX* and converted to Jy sr^{-1}) extracted from Fig. 2a. Regions shown are west of DR21 (**a**), around DR21 (**b**) and DR22 (**c**). The 1.2 mm and 8 μm images have 11″ and 20″ angular resolutions, respectively. The compact cloud fragments discovered in MAMBO images (see Table 1) are labeled and marked by crosses in the gray-scale plot. The infrared sources which coincide with a MAMBO cloud fragment are also indicated. Contour levels are logarithmic and go from 40 to 800 mJy beam^{-1} in **a** and **c**, and from 40 to 4 800 mJy beam^{-1} in **b**.

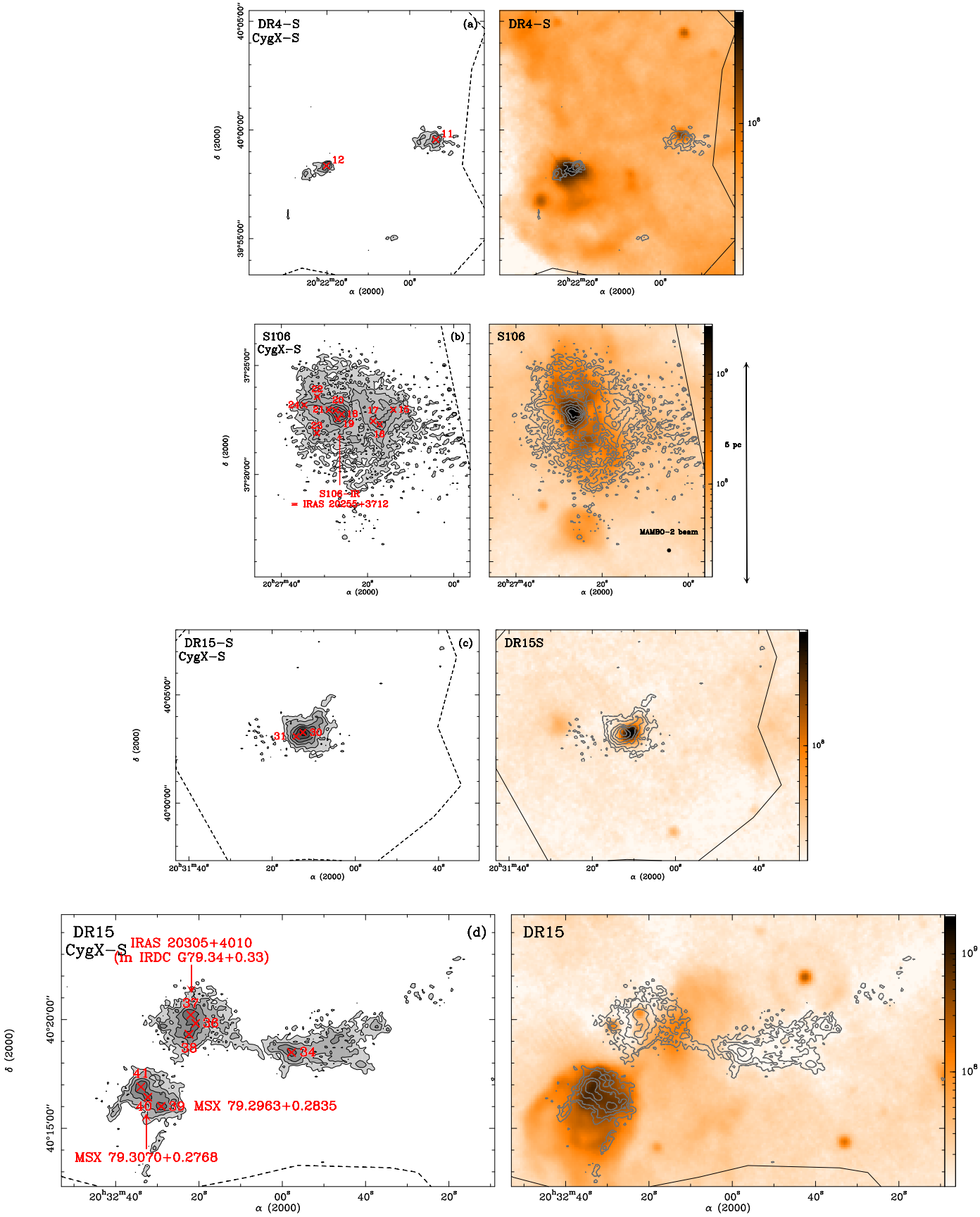

Fig. 4. Same convention as Fig. 3 for MAMBO maps of CygX-South extracted from Fig. 2b. Regions shown are south of DR4 (**a**), around S106 (**b**), south of DR15 (**c**), and around DR15 (**d**). Contour levels are logarithmic and go from 40 to 200 mJy beam^{-1} in **a** and **d**, from 60 to 1 200 mJy beam^{-1} in **b**, and from 40 to 400 mJy beam^{-1} in **c**.

8 μm emission is extinguished by their high-column density, and CygX-N65, which is very weak. The positional accuracy requested between the compact sources of MAMBO-2 and *MSX* is 10″ (i.e. the sum of the maximum pointing errors of both images), which corresponds to 0.08 pc at 1.7 kpc. Such a narrow association is made possible by the small size ($\sim$ 0.1 pc) of the compact cloud fragments extracted from the MAMBO-2 images. In fact if we consider looser associations, many *MSX* point sources lie on and possibly within clumps, at $\sim$ 0.2 pc from the density peaks which we identified as compact fragments (e.g. Figs. 3a-b). We reject these loose associations, unlike previous studies that considered, for example, that CygX-S12 (respectively CygX-S30) and IRAS 20205+3948 (respectively IRAS 20293+3952) coincide (cf. Figs. 4a and 4c, see also Beuther et al. 2002). In fact, these *MSX* point sources lying within dust clumps sometimes coincide with extremely red objects detected by *Spitzer*/IRAC (EROs, Marston et al. 2004, Davis et al. 2007), confirming that (sub)millimeter and infrared surveys generally identify different population of stars in terms of age and/or mass.

Our cross-correlations are illustrated in the right-hand parts of Figs. 3–4 and Figs. 12–14. Their results are given in Col. 8 of Table 1. When there is a coincidence with a *MSX* point source, Col. 8 gives its 21 μm flux as taken from the *MSX* catalog (see Note c for exceptions) and Col. 9 gives the *IRAS* or *MSX* name. Otherwise, when the MAMBO-2 source is not detected or seen in absorption at 8 μm, Col. 8 of Table 1 mentions "–" or "Abs".

With the above selection criteria, 36 compact cloud fragments of Cygnus X (i.e. less than 1/3 of the sample) are associated with mid-infrared emission detected by *MSX*. The other 93 fragments are undetected down to $\sim$ 0.15 Jy at 8 μm and $\sim$ 3 Jy at 21 μm, which are the completeness levels of the *MSX* catalog (MSX C6) in Cygnus X (see Egan et al. 2001; Bontemps et al. in prep.). Some of these sources are even seen in absorption against the diffuse mid-infrared background. Interestingly, some of the Cygnus X fragments which are undetected by *MSX* harbor a weak 24 μm source in *Spitzer* images. To preserve the homogeneity of our study, we do not use this information here.

4.2. Survey for SiO emission

Silicon monoxide (SiO) emission is an excellent tracer of shocked gas, usually associated with molecular outflows (e.g. Ziurys & Friberg 1987; Martín-Pintado et al. 1992; Schilke et al. 1997). SiO may also have been detected in shocks toward hot cores (e.g. Hatchell et al. 2001 and references therein). We have surveyed for SiO(2 – 1) emission by making single pointings toward almost[4] all the most massive ($M_{1.2\,\mathrm{mm}} > 40\ M_\odot$) fragments of Table 1 and a few less massive fragments. Figure 5 and Fig. 15 (only provided electronically) display the SiO(2 – 1) lines for all the observed fragments, ordered by decreasing $M_{1.2\,\mathrm{mm}}$. In Table 3 and for each 1.2 mm compact fragment (Col. 1), we give the peak line temperature (Col. 3), the line width at half maximum (Col. 4), the full line width at the base (Col. 5), and the integrated intensity (Col. 6) of the SiO(2-1) emission. For direct comparison, we list the SiO line parameters scaled to the Cygnus X distance of three nearby protostars which are among the brightest known SiO outflow sources.

Among the 28 most massive fragments whose SiO emission is displayed in Fig. 5, only two (CygX-S18, and CygX-N6) are not detected. This implies a very high detection rate of 93 % (> 79 % when considering the five high-mass fragments which have not been observed), with a typical detection level of $\sim$ 0.15 K km s^{-1} (see Table 3). This detection rate stays high even when considering the observation of the 20 – 40 $M_\odot$ dense cores listed in Table 3. Down to $\sim$ 25 $M_\odot$, the compact fragments of Table 3 that do not have any SiO emission are all associated with infrared point sources: CygX-S18/S106-IR, CygX-N6/IRAS 20343+4129, and CygX-N16/MSX 81.4452+0.7635. This suggests that all massive fragments down to at least 40 $M_\odot$, and maybe 25 $M_\odot$, drive SiO outflows and/or contain hot cores.

In Fig. 5, we show the emission spectra separately for the high-luminosity infrared sources ($\geq 10^3\ L_\odot$) and the massive infrared-quiet cores (cf. their definitions given in Sects. 5.2.2 and 5.3.1). The two groups obviously have different behavior. All infrared-quiet cores are detected in SiO(2-1) and most of them are particulary bright; the averaged peak line temperature and integrated intensity are 0.55 K and 4.6 K km s^{-1}, respectively. In contrast, only a small fraction of the high-luminosity infrared sources show a strong SiO line; the averaged peak line temperature and integrated intensity are 0.22 K and 1.9 K km s^{-1}, respectively. Since only two high-luminosity infrared sources (CygX-N48/DR21 and CygX-N30/W75N) are strong SiO emitters, the contrast is even larger when comparing the median values: 0.7 K km s^{-1} for the high-luminosity infrared sources, and 3.1 K km s^{-1} (i.e. 4.3 times more) for the infrared-quiet cores. The SiO lines of infrared-quiet cores are also 3 to 4 times brighter than the brightest SiO outflows of the nearby low-mass protostars (see Table 3).

Almost all the SiO lines shown in Figs. 5 and 15 display outflow wings with line width at the base of emission that can reach up to $\sim$ 60 km s^{-1}. Among the ten brightest SiO sources, the average of the line width at the base is as high as 41 km s^{-1}, thus clearly suggesting outflow shocks. A few SiO lines might also indicate the presence of at least two emission components: a wide base (due to outflow shocks) and a narrower component which may indicate a contribution of shocks inside a hot core and/or lower velocity outflows. The best examples of two-component lines are those detected toward CygX-S26/AFGL 259, CygX-N44/DR21(OH), and CygX-N48/DR21(OH)-S, while the best example of single-component lines suggestive of a unique powerful outflow are CygX-N46/DR21, CygX-N53, CygX-S30, and CygX-N68.

4.3. Coincidence with radio free-free and maser emission

We have used the SIMBAD[5] database to search for complementary signposts of stellar activity: centimeter free-free emission and OH, H_2O, and CH_3OH masers. SIMBAD gives inhomogeneous information on our sample of 129 compact cloud fragments, since it compiles results of Cygnus X surveys performed with limited angular resolution and high-angular resolution studies made for well-known sources.

Within Table 1, fifteen dense cores coincide with a small-diameter ($\leq$ 10″) source of radio emission detected at 2, 3.6, 6, 11, or 21 cm (e.g. Kurtz et al. 1994;

[4] Three sources (CygX-N32, N47, and S20) are included in beams targeting other fragments (CygX-N30, N46, and S18 respectively). Two sources (CygX-N69 and CygX-S10) were not observed because they are among the lowest-density fragments.

[5] SIMBAD is the reference database for identification and bibliography of astronomical objects, developed and maintained by CDS, Strasbourg.

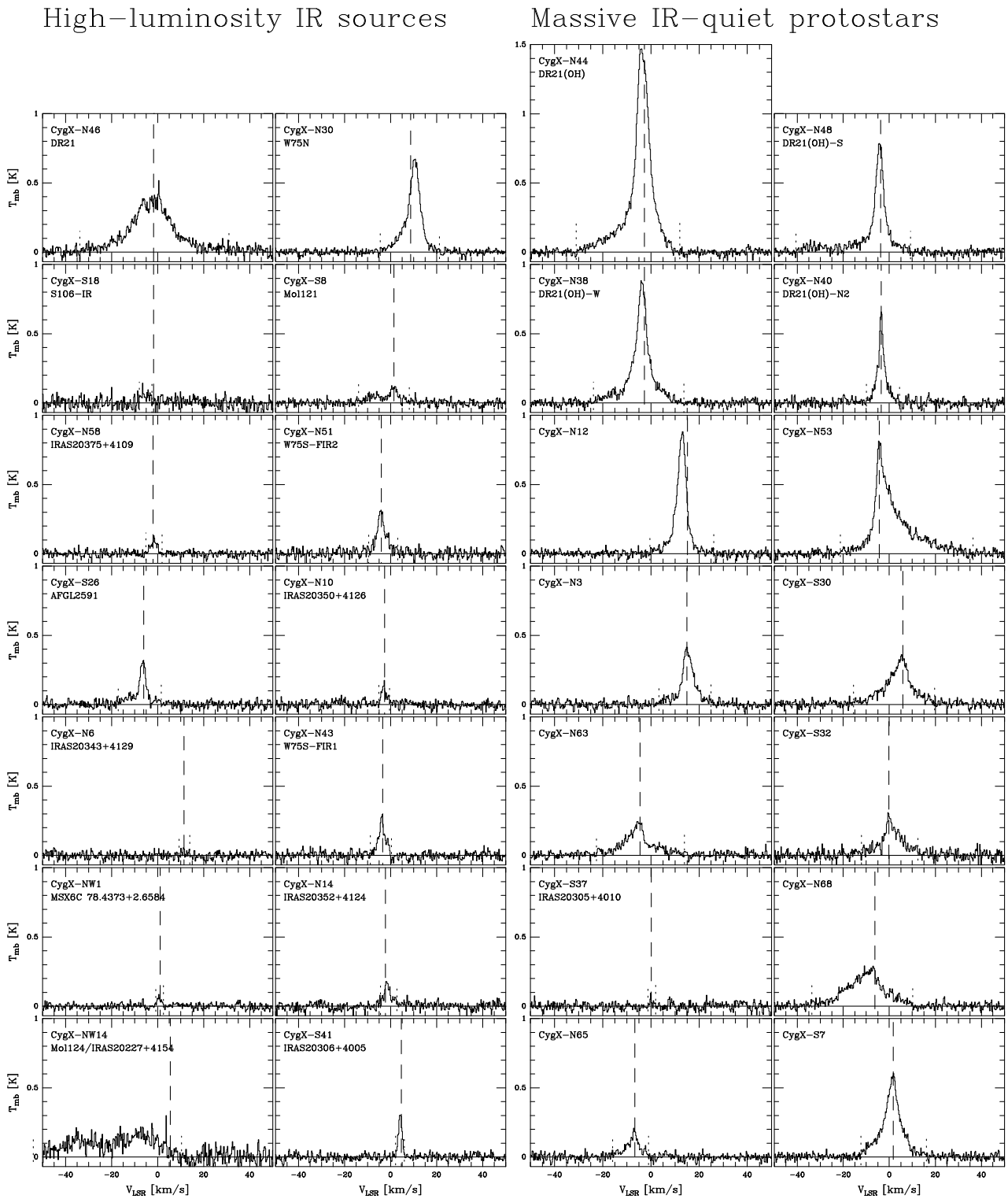

Fig. 5. SiO(2-1) lines observed toward the 28 most massive (> 40 $M_{\odot}$) cloud fragments of Cygnus X: 14 high-luminosity infrared sources on the left and 14 infrared-quiet protostellar cores on the right, both ordered by decreasing $M_{1.2\,\mathrm{mm}}$ from top to bottom. The local velocity at rest of each cloud fragment, as measured by optically-thin tracers, is indicated by a dashed line.

Zoonematkermani et al. 1990). We cannot check the nature of the detected centimeter emissions with the current database, but it most likely corresponds to free-free emissions emitted by H II regions. Furthermore, several 1.2 mm continuum sources coincide with OH, H_2O, and/or CH_3OH maser sources (e.g. Braz & Epchtein 1983; Valdettaro et al. 2001; Pestalozzi et al. 2005). Most of these dense cores are associated with centimeter continuum and/or mid-infrared emission, but one (CygX-N53) is neither a centimeter nor a *MSX* source. In Col. 9 of Table 1, we indicate when some centimeter free-free and/or maser emission is detected toward a Cygnus X dense core.

Table 3. SiO(2-1) observations of the most massive dense cores of Cygnus X compared with the brightest SiO protostellar sources at < 500 pc

Source name	$M_{1.2\,\mathrm{mm}}$ ($M_\odot$)	T_{SiO} (K)	Δv_{FWHM} (km s^{-1})	$\Delta v_{\mathrm{outflow}}$ (km s^{-1})	$\int T_{\mathrm{SiO}}\,dv$ (K km s^{-1})	Possible nature
N46, DR21	< 609 – 949	0.38	16.9	64.8	8.6 ± 0.42	UCH II region
N30, W75N(B)	< 361 – 563	0.65	5.4	25.8	4.7 ± 0.16	hyper compact H II region?
N44, DR21(OH)	446	1.45	6.0	43.0	13.4 ± 0.25	**massive IR-quiet** protostellar core
S18, S106-IR	< 145 – 226	< 0.10	-	-	< 0.15	compact H II region
N48, DR21(OH)-S	197	0.78	4.0	49.7	5.4 ± 0.26	**massive IR-quiet** protostellar core
S8, Mol 121S	< 121 – 188	0.10	4.6	22.1	0.96 ± 0.18	UCH II region
N58, IRAS 20375+4109	< 92 – 144	0.086	3.8	7.1	0.34 ± 0.10	compact H II region
N38, DR21(OH)-W	138	0.86	4.6	37.5	6.8 ± 0.25	**massive IR-quiet** protostellar core
N51, W75S-FIR2	125	0.29	3.6	12.7	1.5 ± 0.19	**high-luminosity IR** protostellar core
S26, AFGL2591	< 80 – 124	0.30	2.8	18.7	1.5 ± 0.19	UCH II region
N40, DR21(OH)-N2	106	0.63	2.6	14.4	2.3 ± 0.18	**massive IR-quiet** protostellar core
N12	86	0.87	4.0	26.5	4.7 ± 0.21	**massive IR-quiet** protostellar core
N53	85	0.80	6.4	57.6	8.9 ± 0.31	**massive IR-quiet** protostellar core
N3	84	0.40	4.8	21.5	2.6 ± 0.21	**massive IR-quiet** protostellar core
S30	82	0.32	9.3	35.2	3.9 ± 0.26	**massive IR-quiet** protostellar core
N10, IRAS 20350+4126	< 52 – 81	0.12	2.4	4.7	0.35 ± 0.10	UCH II region?
N6, IRAS 20343+4129	44-68	< 0.07	-	-	< 0.10	**high-luminosity IR** protostellar core
N43, W75S-FIR1	66	0.25	3.4	9.1	0.94 ± 0.15	**high-luminosity IR** protostellar core
NW1, IRAS20178+4046	< 38 – 59	0.05	2.6	3.4	0.15 ± 0.06	UCH II region?
N63	58	0.23	7.2	36.5	2.6 ± 0.23	**massive IR-quiet** protostellar core
S32	54	0.29	6.2	24.6	2.4 ± 0.28	**massive IR-quiet** protostellar core
N14, IRAS 20352+4124	50	0.16	2.4	7.1	0.61 ± 0.13	**high-luminosity IR** protostellar core
NW14, Mol124	32-50	0.16	41.6	64.4	5.8 ± 0.76	**high-luminosity IR** protostellar core
S37, IRAS 20305+4010	45	0.05	-	3.2	0.09 ± 0.09	**massive IR-quiet** protostellar core
N68	44	0.27	13.7	43.8	4.6 ± 0.25	**massive IR-quiet** protostellar core
S41, IRAS 20306+4005	27-42	0.30	2.0	8.2	0.61 ± 0.09	**high-luminosity IR** protostellar core
N65	41	0.19	3.8	16.9	1.06 ± 0.16	**massive IR-quiet** protostellar core
S7	40	0.58	6.0	28.4	5.1 ± 0.23	**massive IR-quiet** protostellar core
NW2	36	0.10	-	2.0	0.18 ± 0.09	IR-quiet protostellar core
S43	35	0.16	2.2	6.1	0.59 ± 0.13	IR-quiet protostellar core
N24	34	0.09	4.7	5.1	0.39 ± 0.10	IR-quiet protostellar core
NW5, LkHA 225S	22-34	0.045	-	14.9	0.69 ± 0.26	infrared protostellar core
N60	30	0.08	2.0	4.5	0.20 ± 0.10	IR-quiet protostellar core
N16, MSX 81.4452+0.7635	29	< 0.09	-	-	< 0.12	infrared protostellar core
N28	27	0.09	1.8	3.5	0.25 ± 0.09	IR-quiet protostellar core
N62	27	0.10	2.6	8.5	0.42 ± 0.11	IR-quiet protostellar core
S16	24	0.10	2.6	14.5	0.51 ± 0.13	IR-quiet protostellar core
N18	23	< 0.08	-	-	< 0.11	?
N59	20	< 0.08	-	-	< 0.11	?
NW9, IRAS 20216+4107	19	< 0.10	-	-	< 0.15	infrared protostellar core
L1448-MM @ 1.7 kpc	-	-	-	~ 140	~ 1.4[(a)]	low-mass class 0 protostar
L1157-MM @ 1.7 kpc	-	-	-	~ 25	~ 1.8[(b)]	low-mass class 0 protostar
Orion-IRc2 @ 1.7 kpc	-	-	-	~ 74	~ 9.2[(c)]	high-mass protostar

[a] Intensity which has been distance-corrected (extrapolation from 300 pc to 1.7 kpc) using values from Table 2 of Nisini et al. (2007) and excluding R4 which would fall outside the beam.
[b] Intensity which has been distance-corrected (extrapolation from 440 pc to 1.7 kpc) using values from Table 3 of Nisini et al. (2007) and summing up B0 and B1 components.
[c] Intensity which has been distance-corrected (extrapolation from 450 pc to 1.7 kpc) using the spectrum of Fig. 1 in Ziurys & Friberg (1987).

5. Discussion

5.1. A sample of high-density cores

Our 1.2 mm continuum imaging of the Cygnus X molecular cloud complex gives a complete view of the structure of its highest-column density portions, with spatial scales ranging from 0.03 pc (deconvolved from the beam) to 3 pc. According to the terminology used for nearby molecular clouds (e.g. Williams et al. 2000), it covers scales typical for dense cores (~ 0.1 pc) and clumps (~ 1 pc). The 129 compact cloud fragments identified in Cygnus X have sizes ranging from 0.03 to 0.3 pc with a mean size of ~ 0.1 pc (see Sect. 3.2 and Table 1). They should therefore be called "dense cores". The 40 larger-scale structures of Table 2 have typical sizes of ~ 0.7 pc; we will call them "clumps". In Table 4, we give the mean properties of the Cygnus X dense cores and clumps and compare them with those of a few representative studies (Motte et al. 1998; Ward-Thompson et al. 1999; Beuther et al. 2002; Rathborne et al. 2006). In Fig. 6a-b, we plot the mass and density distributions of these 1.2 mm sources samples.

The typical size of the Cygnus X dense cores is 5 to 10 times smaller than the average cloud structures identified by single-

Table 4. Mean properties of the Cygnus X clumps and cores compared with millimeter cloud structures of a few reference studies

	HMPOs clumps	IRDCs clumps	CygX clumps (all / starless)	Cygnus X dense cores	> 40 $M_\odot$ CygX dense cores	Nearby, low-mass dense cores	ρ Oph condensations
FWHM [a] size (pc)	0.5	0.5	0.68 / 0.78	0.10	0.13	0.08	0.007
Mass[b] $M_{1.2\,\mathrm{mm}}(M_\odot)$	290	150	1000 / 780	24	91	4.7	0.15
$< n_{\mathrm{H_2}} >^c$ ($\mathrm{cm^{-3}}$)	8.5×10^3	5.9×10^3	1.4×10^4 / 6.7×10^3	1.1×10^5	1.9×10^5	3.5×10^4	1.9×10^6
Number of sources	69[e]	190	40 / 10	128	33	22	60
References[d]	(1)	(2)	(3)	(3)	(3)	(4), (5)	(5)
Distance (kpc)	0.3-14	1.8-7.1	1.7	1.7	1.7	0.14-0.44	0.14

(a) Deconvolved *FWHM* sizes derived from a 2D-Gaussian fit, except for HMPOs and IRDCs for which sizes are taken from Table 1 of Beuther et al. (2002) (mean estimates are taken when the distance is unknown) and Table 3 of Rathborne et al. (2006).
(b) Mass consistently estimated from the 1.2 mm integrated flux using Eq. (1). The mass values of Beuther et al. (2002) have been recalculated using $\kappa_{1.2\,\mathrm{mm}} = 0.01\ \mathrm{cm^2\,g^{-1}}$ but those of nearby, low-mass dense cores and ρ Oph condensations are kept while they assume $\kappa_{1.2\,\mathrm{mm}} = 0.005\ \mathrm{cm^2\,g^{-1}}$.
(c) Volume-averaged density homogeneously recalculated using Eq. (2) for every list of sources.
(d) References: (1) Beuther et al. (2002); (2) Rathborne et al. (2006); (3) this paper; (4) Ward-Thompson et al. (1999); (5) Motte et al. (1998).
(e) We limit our comparison to the main HMPOs components, which are the most likely progenitors of high-mass stars.

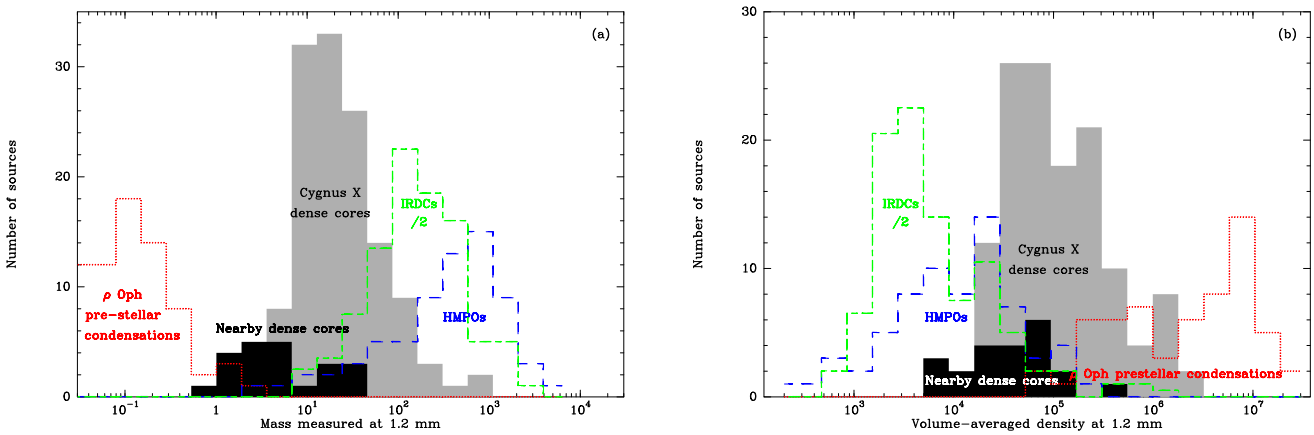

Fig. 6. Distribution of mass (**a**) and volume-averaged density (**b**) of the Cygnus X dense cores compared to those of clumps hosting high-luminosity protostars (main component of HMPOs, Beuther et al. 2002) and clumps referred to as IRDCs (Rathborne et al. 2006). The Cygnus X histograms are also compared to density spectra of nearby dense cores (Motte et al. 1998; Ward-Thompson et al. 1999) and ρ Oph condensations (Motte et al. 1998).

dish studies of high-mass star-forming regions (see Table 4 and also Reid & Wilson 2005; Hill et al. 2005). Using the terminology mentioned above, HMPOs (for high-mass protostellar objects, Beuther et al. 2002) and IRDCs (for infrared dark clouds, e.g. Rathborne et al. 2006) are actually "clumps". We are here able to reach the scale of dense cores because Cygnus X is one of the closest high-mass star-forming regions, our MAMBO-2 survey has a good spatial resolution, and we deliberately focus on high-density cloud structures. As a consequence of their small sizes, the Cygnus X dense cores have masses ($4-950\ M_\odot$, see Table 1) which are up to one order of magnitude smaller than those obtained by Beuther et al. (2002) and Rathborne et al. (2006) (see Table 4 and Fig. 6a). In contrast, Cygnus X dense cores have densities averaged over their *FWHM* size ($1 \times 10^4 - 2 \times 10^6\ \mathrm{cm^{-3}}$) which are more than *one order of magnitude higher* than those of HMPOs and IRDCs (cf. Table 4 and Fig. 6b). As interesting illustrations, the Cygnus X HMPOs called IRAS 20343+4129 and IRAS 20293+3952 (Beuther et al. 2002) are twice as large and 7 times less dense than the dense cores we have identified within them (see CygX-N5, CygX-N6 and CygX-S30 in Table 1).

On average, the Cygnus X dense cores are a factor of 5 more massive and a factor of 3 denser than nearby dense cores identified by Motte et al. (1998) and Ward-Thompson et al. (1999) (see Table 4 and Figs. 6a-b). The latter sample includes isolated pre-stellar cores located at 140-440 pc from the Sun, and all the protocluster dense cores of the ρ Ophiuchi main cloud which are either pre-stellar or already forming low-mass stars. Statistically, studying the Cygnus X region gives access to dense cores which are one to two orders of magnitude more massive than those observed in nearby regions. The 33 most massive compact cloud fragments of Cygnus X (i.e. with masses larger than 40 $M_\odot$, see Table 3) already have 19 times more mass than the dense cores of low-mass star-forming regions (cf. Table 4). Thus, they do not have any equivalent in the nearby star-forming regions and represent good candidate sites for forming intermediate- to high-mass stars.

In terms of average density, Cygnus X dense cores are intermediary cloud structures between nearby dense cores and condensations in the ρ Ophiuchi main cloud (cf. Table 4 and Fig. 6b). This result suggests that the efficiency of mass transfer from the gas reservoir to the star(s) is high. Indeed, the star formation efficiency estimated in the ρ Ophiuchi dense cores is

$\sim$ 31% over 10^6 yr (Bontemps et al. 2001), and the good agreement in ρ Oph between the pre-stellar condensation mass spectrum and the stellar IMF suggests an efficiency of 50% – 100% (Motte et al. 1998; Bontemps et al. 2001). While the low-mass starless condensations are believed to be the direct progenitors of single stars, the Cygnus X dense cores will probably form small groups of stars. The large mass of the Cygnus X dense cores, compared to that of nearby dense cores and ρ Oph condensations, argues for the formation of intermediate- to high-mass stars (cf. Fig. 6a). With their high density and small size, the Cygnus X dense cores can probably be seen as the inner part of clumps/protoclusters over which the stellar IMF does not globally apply. Therefore, we may expect that the $> 40\ M_\odot$ dense cores of Cygnus X have a high probability of forming $10-20\ M_\odot$ of stars, including at least one high-mass star. The detection of maser emission toward a few moderate-mass ($\sim 20\ M_\odot$) dense cores that remain weak at mid-infrared wavelength (cf. Wyrowski et al. in prep.) suggests that the $> 40\ M_\odot$ limit for a Cygnus X dense core to host a high-mass protostar is reasonable.

5.2. The high potential of Cygnus X dense cores to form massive stars

The Cygnus X molecular complex has already formed generations of high-mass stars, since it contains several OB associations (Uyaniker et al. 2001) and numerous H II regions (Wendker et al. 1991). We here discuss its ability to form high-mass stars in the near future by making a census of embedded H II regions (Sect. 5.2.1), high-luminosity protostellar cores (Sect. 5.2.2), and massive infrared-quiet cores which are bright in SiO (Sect. 5.2.3). We summarize in Table 5 the number of objects found at various stages of the high-mass star formation process.

5.2.1. Embedded H II regions

Within our sample of high-density cores, we identify 15 embedded H II regions from their bright infrared and centimeter continuum emissions (see Cols. 8-9 of Table 1). Most of them are already recognized as compact or ultra-compact H II regions (Downes & Rinehart 1966; Haschick et al. 1981; Kurtz et al. 1994; Molinari et al. 1998b; Trinidad et al. 2003). Five others (CygX-N47/DR21-D, CygX-N58/IRAS 20375+4109, CygX-S18/S106-IR, S20, CygX-S27/MSX 77.9550+0.0058) coincide with radio centimeter sources from the 1.4 GHz Galactic Plane Survey (Zoonematkermani et al. 1990) or old centimeter maps (Harris 1973; Pipher et al. 1976). As expected, observations of high-density tracers such as CS, NH_3 line and 350 μm continuum made toward these 1.2 mm sources suggest some free-free contamination (e.g. Motte et al. in prep.).

Despite harboring an H II region, most of these massive young stellar objects are embedded and some of them (e.g. CygX-N46/DR21, CygX-N30/W75(N), CygX-S/AFGL 2591) even show high levels of ongoing star formation activity, such as maser emission and/or powerful outflow shocks (see Tables 1 and 3 and Figs. 5 and 8). In agreement with these H II regions being compact, ultra-compact, or even hyper-compact, our 1.2 mm study is sensitive to young and thus "embedded H II regions".

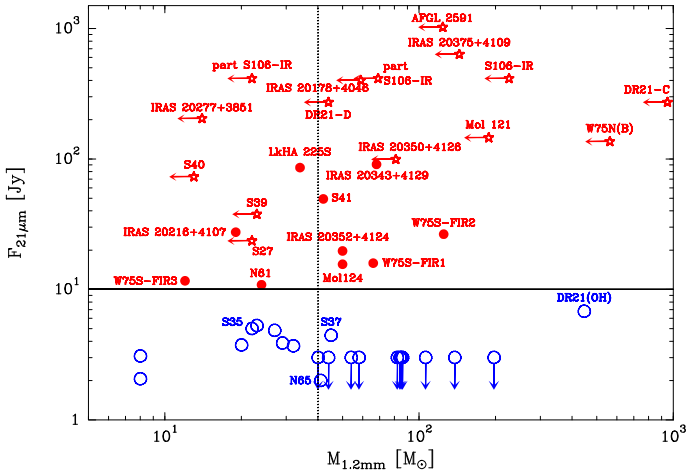

Fig. 7. Separating the high-luminosity ($> 10^3\ L_\odot$) sources from infrared-quiet cores using their 21 μm flux (limit set to 10 Jy). In Cygnus X, 15 UCH II regions (red star-like markers) and 10 infrared protostars (red filled circles) have high luminosity. A few infrared-quiet cores (blue open circles) are weak *MSX* sources (like DR21(OH)) but most of them remain undetected (those more massive than 40 $M_\odot$ are plotted here).

5.2.2. "High-luminosity infrared sources"

Dense cores which are luminous at infrared wavelengths are usually considered to be the best candidates to be (or to host) high-mass protostars (e.g. Wood & Churchwell 1989). Following a similar philosophy, we qualify as "high-luminosity infrared sources" those Cygnus X dense cores with bolometric luminosity larger than $10^3\ L_\odot$, which corresponds to that of a B3 star on the main sequence. This luminosity converts into a *MSX* 21 μm flux of $\sim$ 10 Jy, assuming that the luminosity of high-mass protostars is dominated by their mid- to far-infrared luminosity and their average colors are defined by Wood & Churchwell (1989) (see their Table 1). In practice, we estimate the total flux in the *IRAS* bands using the simplified formulae[6] of Casoli et al. (1986) and the Wood & Churchwell (1989) colors to express this total flux as a function of the single *IRAS* 25 μm flux. We finally convert the 25 μm flux into an expected *MSX* flux at 21 μm by an interpolation between 25 and 12 μm using the Wood & Churchwell color. For $d = 1.7$ kpc, we finally estimate a typical *MSX* flux at 21 μm of $\sim$ 10 Jy $\times (L_{IRAS}/10^3\ L_\odot)$ for a B3 protostar. Figure 7 displays the 21 μm flux detected toward Cygnus X dense cores as a function of their mass. With a 10 Jy limit in Fig. 7, we detect all the embedded H II regions plus 10 sources which are "high-luminosity infrared protostellar cores". Three of the latter are associated with OH, H_2O, and/or CH_3OH maser emission: CygX-N43/W75S-FIR1, CygX-N44/DR21(OH), and CygX-NW5/LkA 225S.

The high-luminosity infrared sources of the present Cygnus X survey are mostly *IRAS* sources fulfilling the Wood & Churchwell (1989) criteria for UCH II regions or objects in an earlier stage of high-mass star formation. Many of them were already identified as high-mass protostellar sources: e.g. W75S-FIR1 and -FIR2 (see Chandler et al. 1993a) and IRAS 20343+4129 and IRAS 20216+4107 (Beuther et al. 2002).

[6] $F_{IRAS} = 1.75\times10^{-13}\ \mathrm{W\,m^{-2}}\times(S_{12}/0.79+S_{25}/2+S_{60}/3.9+S_{100}/9.9)$ with S_{12}, S_{25}, S_{60}, S_{100} expressed in Jy.

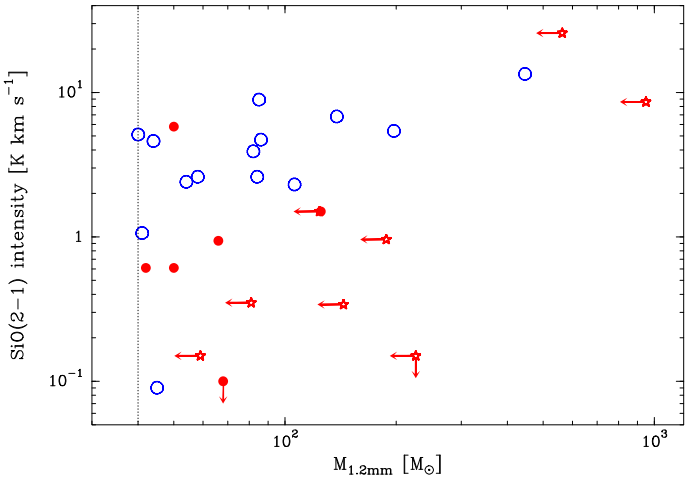

Fig. 8. Integrated intensity of SiO(2-1) detected toward the Cygnus X dense cores more massive than 40 $M_\odot$, as a function of their mass. Infrared-quiet cores (blue open circles) are definitely stronger in SiO than the high-luminosity protostellar cores (red filled circles) and UCH II (red star-like markers).

5.2.3. Strong SiO emission as a probe for high-mass protostars

In contrast to high-luminosity infrared sources, massive infrared-quiet cores are not all expected to host high-mass protostars. It is therefore interesting and somewhat surprising to find that all of them are bright SiO emitters (cf. Table 3 and Fig. 5). As shown below, their SiO(2-1) lines are well interpreted as due to a powerful outflow that is probably driven by one high-mass protostar.

As shown in Fig. 8, which presents the SiO intensity of the Cygnus X dense cores versus their mass, the SiO lines detected for infrared-quiet cores are several times brighter than those observed for the high-luminosity sources. As an example, the well-recognized UCH II region CygX-S26/AFGL 2591 is weaker (in SiO) than a completely unknown source such as CygX-N53. Since (SiO) outflows are tracing the accretion process (see Bontemps et al. 1996), this result suggests that massive infrared-quiet cores are in a more active accretion phase than high-luminosity infrared sources. Furthermore, the SiO emission of massive infrared-quiet cores is several times stronger than the most extreme SiO shocks associated with nearby low-mass class 0 protostars (see e.g. Table 3). This suggests that the infrared-quiet cores host either a clear single SiO outflow driven by a high-mass protostar, or a group of SiO outflows as extreme as those of L1448-MM or L1157-MM. Quantitatively the mean SiO brightness of the massive infrared-quiet cores in Cygnus X would require the summation of two low-mass class 0s driving extreme SiO outflows (and up to 5 in the case of CygX-N53). This is rather improbable, since we evaluate the occurence of such SiO outflows to be of the order of 6% (2 out of 35 class 0s known at $d < 500$ pc; e.g. André et al. 2000). Statistically, the summation of several tens of low-mass class 0s would be required to explain the bright SiO emissions observed here. The SiO outflows of these infrared-quiet cores better resemble that of the high-mass protostar Orion-IRc2 (see Ziurys & Friberg 1987 and Table 3). These intensity comparisons suggest that the infrared-quiet protostellar cores of Cygnus X are much more active (in star formation) than nearby low-mass protostars, and that a large fraction of them should host high-mass analogs of class 0s.

The profile of the SiO lines provides us with useful additional constrains. Half of the infrared-quiet protostellar cores in Table 3 (CygX-N53, N63, N68, S30, S32 and possibly N3, N65, S7) show clear and smooth outflow wings in their SiO line profiles. These profiles are so clean that it can be taken as a good indication that the SiO emission is dominated by a single SiO outflow which, in turn, has to be powered by a high-mass protostar. Four infrared-quiet protostellar cores (CygX-N44/DR21(OH), CygX-N48/DR21(OH)-S, CygX-N38/DR21(OH)-W, and CygX-N12) have a profile which is more indicative of two emission components: a strong narrow line plus a line with large wings (see Sect. 4.2). This can arise from two different SiO outflows which would both still be powerful, or from a single outflow composed of two main velocity patterns in the SiO shocks. An alternative interpretation is that, besides the outflow, some shocks associated with a hot core would be detected as a narrow SiO line component.

Therefore, the > 40 $M_\odot$ dense cores of Cygnus X all have a high probability of containing (at least) one high-mass protostar, whether or not they are bright infrared sources. Our selection of extreme-density cores has thus proven to be very efficient in locating sites of future formation of high-mass stars.

5.3. "Massive infrared-quiet protostars": definition and lifetime

5.3.1. Definition

We define as "massive infrared-quiet protostellar cores" the Cygnus X dense cores that are more massive than 40 $M_\odot$, weak at infrared wavelengths (i.e. $<$ 10 Jy at 21 μm), but present some signposts of stellar activity. Table 1 provides a list of 33 dense cores more massive than 40 $M_\odot$ (see also Table. 4) and Fig. 7 allows the identification of "high-luminosity infrared sources" (see also Sect. 5.2.2). The 17 remaining dense cores should either be infrared-quiet protostellar cores or starless cores. Among them, four are already identified as protostellar cores by their weak *MSX* detection and/or their association with masers: CygX-N44/DR21(OH), CygX-N65, CygX-S37/IRAS 20305+4010, and CygX-N53. The majority of the 17 massive infrared-quiet cores have been surveyed in SiO(2-1); 14 positions are listed in Table 3 and CygX-N32 is included in the beam targeting CygX-N30. The brightness and line shape of their SiO emission prove that the infrared-quiet cores are all protostellar in nature and that they probably host a high-mass protostar (see Sect. 5.2.3).

5.3.2. Lifetime of high-mass protostars

Our study supports the existence of massive infrared-quiet protostars, overlooked by infrared-based surveys (see Figs. 7–8). It provides a sample of (mostly) new massive infrared-quiet protostellar cores which contain high-mass protostars. We still lack the necessary angular resolution to identify individual high-mass protostars, but the characteristics of each Cygnus X dense core more massive than 40 $M_\odot$ are believed to be shaped by those of a single embedded high-mass protostar (cf. Sects. 5.1 and 5.2.3). With this assumption, we give the first lifetime estimates for this new population of high-mass protostars, assuming a constant star formation rate in Cygnus X over the past 1-2 Myr.

Since our sample of Cygnus X dense cores is complete for embedded, massive, young stellar objects, we can statistically estimate the relative lifetimes of massive infrared-quiet protostars and high-luminosity infrared sources (including in-

Table 5. Massive young stellar objects found in Cygnus X at various stages of the high-mass star formation process

	Starless clumps	Pre-stellar cores	Massive IR-quiet protostars	High-luminosity IR protostars	H II regions	OB stars
Number in Cygnus X	10	≤ 1	17	25	~ 800	2600 ± 1000
References	this paper	this paper	this paper	this paper	Wendker et al. 1991	Knödlseder 2000
Statistical lifetime[a]	$\sim 7 \times 10^3$ yr	$\leq 8 \times 10^2$ yr	$\sim 1.3 \times 10^4$ yr	$\sim 1.9 \times 10^4$ yr	$\sim 6 \times 10^5$ yr	$(2 \pm 1) \times 10^6$ yr
$< n_{H_2} >$	6.7×10^3 cm^{-3}	$\sim 1.5 \times 10^5$ cm^{-3}	1.7×10^5 cm^{-3}			
Free-fall time[b]	4×10^5 yr	$\sim 9 \times 10^4$ yr	8×10^4 yr			
Number in Orion	?	?	~ 1	~ 1	~ 6	~ 81

(a) Lifetime of massive starless clumps, pre-stellar cores, infrared-quiet protostars, high-luminosity infrared sources, and H II regions measured relative to the known age of OB stars (cf. Hanson 2003) using the census given in Line 3.

(b) Free-fall time measured from the mean values of the volume-averaged density given in Line 6: $t_{\text{free-fall}} = \sqrt{\frac{3\pi}{32\,G\,<\rho>}}$.

frared protostars and embedded H II regions). The separation of infrared sources between embedded H II regions and high-luminosity infrared cores is not final since centimeter continuum follow-up observations are necessary, and a low-level of centimeter free-free detection might be indicative of outflow shocks rather than H II regions. In the following discussion, we therefore treat cores hosting high-luminosity infrared sources and possibly protostars as a single population. According to the numbers of high-luminosity infrared sources and massive infrared-quiet protostars given in Table 5 (and taken from Sects. 5.2.1–5.2.2 and Sect. 5.3.1), the infrared-quiet protostellar phase of high-mass stars might last as long as their better-known infrared-bright protostellar (or embedded H II) phase. This result is in disagreement with the idea that high-mass protostars are very luminous from the very first stage of their evolution and thus that their infrared-quiet phase is very short-lived.

Table 5 gives our current estimates of the number of massive young stellar objects forming and stars already formed in Cygnus X. The number and age of OB stars in Cygnus X are taken to be those of the Cyg OB2 association (Knödlseder 2000; Hanson 2003), increasing uncertainties to take into account the other (smaller) OB associations which have different ages (Uyaniker et al. 2001). The number of H II regions is crudely given by the numbers of centimeter free-free sources observed in Cygnus X (Wendker et al. 1991). The statistical lifetimes of high-mass protostars derived relative to the number of OB stars give a time range of $(0.5 - 3.1) \times 10^4$ yr for the infrared-quiet protostellar stage and $(1.2 - 7.9) \times 10^4$ yr for the complete protostellar stage (see also Table 5). For the sake of comparison, the statistical lifetime measured for the high-mass protostellar phase in Cygnus X ($\sim 3.2 \times 10^4$ yr) is one order of magnitude smaller than the typical age of nearby, low-mass class I protostars (e.g. Kenyon & Hartmann 1995) and more closely resembles that of low-mass class 0s (cf. André et al. 2000).

Figure 9 displays the number of high-mass protostars, H II regions and OB stars (i.e. objects in the three main evolutionary phases) as a function of the time elapsed since the beginning of the protostellar collapse (i.e. since the formation of a hydrostatic stellar embryo). Absolute lifetimes of the high-mass protostellar phase (encompassing both the infrared-quiet and the high-luminosity infrared protostellar phases) as well as those of the high-mass starless phases can be roughly estimated from their free-fall dynamical timescales. Table 5 gives the estimates we made using the mean values of the volume-averaged density of massive dense cores observed in Cygnus X. The most massive dense cores of Cygnus X should thus collapse in a free-fall time of $\sim 8 \times 10^4$ yr, which is taken to be the end of the high-mass

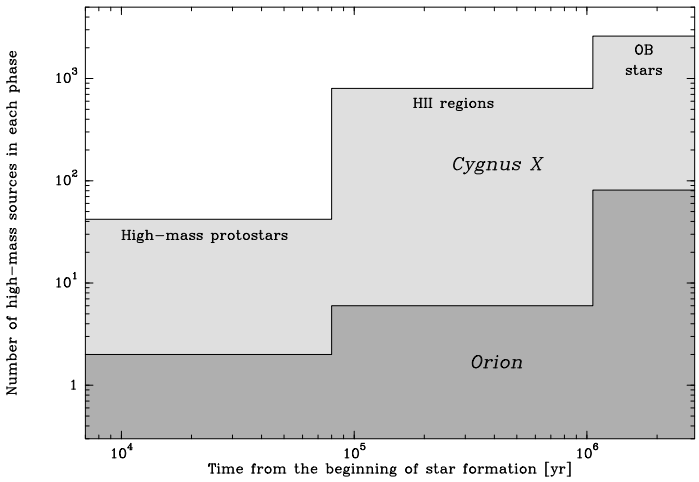

Fig. 9. Number of massive young stellar objects as a function of the time elapsed since the beginning of the protostellar collapse in Cygnus X and Orion. The age estimates (also given in Sect. 5.3.2) are *not* statistical, in order to have the X-axis and Y-axis independent.

protostellar phase in Fig. 9. The H II regions phase should last for several times the typical lifetime of UCH II regions ($\sim 10^5$ yr, cf. Wood & Churchwell 1989), starting in Fig. 9 at the end of the protostellar phase. The free-fall time of high-mass protostars in Cygnus X agrees, within a factor of 3, with the statistical lifetimes of the complete population of high-mass protostars (including both infrared-quiet and high-luminosity infrared protostars) derived relative to the number of OB stars (see Table 5).

To compare Cygnus X to Orion, Table 5 makes the census of all massive young stellar objects known in Orion, and Fig. 9 shows their distribution as a function of time. The number of high-mass stars (down to B3 spectral type) within all the Orion OB associations is measured by Brown et al. (1994), while the H II regions are associated with the well-known reflection nebulae M42, NGC 2024, NGC 1977, M43, NGC 2068, and NGC 2071. One source could qualify as a high-luminosity infrared protostar (Orion-IRC2) and another as a massive infrared-quiet protostar (OMC1-S). Interestingly, the massive young stellar objects forming, and stars formed, in Cygnus X are 20 times more numerous than in Orion (see Table 5), in good agreement with the mass ratio (13) of the Cygnus X and Orion cloud complexes.

5.4. Where is the pre-stellar phase of massive star formation?

Among the 33 most massive ($\geq$ 40 $M_\odot$) dense cores of Cygnus X, no starless cores are found, with the possible exception of CygX-N69 which was not selected for SiO observations because of its relatively large size and corresponding low-density ($\sim 10^4$ cm^{-3}). This non-detection of starless cores means that high-mass pre-stellar cores, if they exist, are short-lived ($< 10^3$ yr, see Table 5). This is particularly surprising since the lifetime of pre-stellar cores and condensations in nearby, low-mass star-forming regions is more than two orders of magnitude longer ($1 - 4 \times 10^5$ yr, e.g. Onishi et al. 2002; Kirk et al. 2005; André et al. 2007). Below, we consider two interpretations: either the star formation activity of Cygnus X is not continuous (see Sect. 5.4.1) or massive pre-stellar clumps are dynamically evolving into protostars (see Sect. 5.4.2).

5.4.1. Star formation in Cygnus X cannot be caused by a burst

If the Cygnus X molecular complex were experiencing a sudden burst of star formation, it might be due to the interaction with the H II regions and/or OB associations, including the Cyg OB2 cluster. In this case, we expect differences in the concentration of gas and in the population of young stellar objects in the CygX-North and CygX-South regions.

Evidence shows that the concentration of gas is different in CygX-North and CygX-South. The CO survey of Schneider et al. (2006), the present MAMBO-2 maps, and our small-scale analysis trace various cloud structures (see Sects. 3.1–3.2). We can thus measure the gradual concentration of molecular clouds (0.5–50 pc scales), first into 0.1–5 pc scales, and then into 0.1 pc dense cores. In CygX-North (280×10^3 $M_\odot$, cf. Schneider et al. 2006), the concentration factor is 8 for each step while in CygX-South (480×10^3 $M_\odot$) it is 18 for each step. Therefore, when considering the mass involved in dense cores, the CygX-North region is 5 times more concentrated (CO clouds concentrate into 0.1 pc cores with an efficiency of $\sim$ 1.5%) than CygX-South (concentration efficiency of $\sim$ 0.3%). This suggests that CygX-North could be 5 times more efficient in forming dense cores, and possibly forming stars, than CygX-South.

In contrast, the relative numbers of "high-luminosity infrared sources" versus "massive infrared-quiet protostellar cores" are identical (within our large error bars) in both regions. Moreover, other generations of (massive) young stars have already formed nearby (see e.g. the *MSX* sources at $\sim$ 0.2 pc from the dense cores). The agreement between the free-fall lifetime and the statistical lifetime of high-mass protostars relative to OB stars also suggests that star formation has been continuous, at least over the past $\sim 10^6$ yr (see also Fig. 9). Therefore, it is highly improbable that Cygnus X is currently experiencing a burst of star formation.

5.4.2. Is the star formation in Cygnus X dynamic?

The present study fails to find a single good candidate for being a pre-stellar dense core, i.e. a starless cloud structure with a $\sim$ 0.1 pc size and a $\sim 10^5$ cm^{-3} volume-averaged density, which is gravitationally bound. This does not preclude, however, the existence of smaller and denser pre-stellar condensations ($\sim$ 0.01 pc size and $\sim 10^6$ cm^{-3} density according to Motte et al. 1998, see Table 4) within the Cygnus X protostellar cores. On the other hand, we have identified 10 clumps which may be starless ($\sim$ 0.8 pc size and 7×10^3 cm^{-3} density, see Tables 2 and 4). The Virial mass of these clumps ($M_{\rm vir} = 3R\sigma^2/G$, Bertoldi & McKee 1992) are estimated from the N_2H^+ linewidth measured at their peak location (Schneider et al. in prep.) and the *FWHM* size given in Table 2; they suggest that most of these clumps are close to being gravitationally bound.

From the numbers of starless clumps and pre-stellar cores detected in Cygnus X and compared to the numbers of OB stars, we statistically estimate their lifetimes to be $\sim 10^4$ yr and $< 10^3$ yr, respectively (see Table 5). These lifetime values are considerably smaller (by factors of 60-110) than the free-fall times we estimated. They are also shorter than the lifetimes observed in nearby regions that form mostly low-mass stars, since starless cloud structures with volume-averaged densities of $\sim 10^3$ cm^{-3} and $\sim 10^4$ cm^{-3} have pre-stellar lifetimes of $\sim 10^6$ yr and $\sim 10^5$ yr (see Fig. 11 of Kirk et al. 2005 and references therein). Therefore, massive pre-stellar cores seem to be short-lived or even transient cloud structures compared to nearby low-mass pre-stellar cores, to high-mass protostars, and to massive starless clumps.

A dynamical process should thus be acting to create pre-stellar condensations from starless clumps. It should be supersonic to concentrate mass from densities of 7×10^3 cm^{-3} to 2×10^5 cm^{-3} in a time as short as, or even shorter than, the free-fall timescale. Similarly short lifetimes are theoretically expected in molecular clouds where highly turbulent processes dominate and pre-stellar cores are magnetically supercritical (e.g. Vázquez-Semadeni et al. 2005). Such dynamical processes are also necessary for the protostellar lifetime to last for only one free-fall time (see Table 5) and, consequently, for the accretion to be strong enough ($\sim 10^{-3}$ $M_\odot$ yr^{-1}) to overcome the radiation pressure and form a high-mass star. In fact, the DR21 filament is observed to undergo a global supersonic collapse, possibly due to a strong external compression (Chandler et al. 1993b; Motte et al. 2005). This is encouraging but it remains to be verified whether such a dynamical process acts throughout the complex.

Taken together, the lifetimes measured here suggest a faster evolution (by a factor 10 at least) of the pre-stellar and protostellar phases of high-mass stars compared to those typically found for nearby, low-mass stars. Molecular clouds harboring high-mass star formations should thus be quantitatively different in terms of e.g. density and kinematics than those of our close neighborhood.

6. Conclusions

In order to improve our knowledge of the high-mass star formation process, we started an unbiased search for its earliest phases, i.e. the high-mass analogs of low-mass pre-stellar cores and class 0 protostars. One of the best targets for such a study is Cygnus X, which we recently recognized as the richest molecular and H II complex at less than 3 kpc (it is located at 1.7 kpc from the Sun). We have therefore made a complete 1.2 mm continnum survey of the Cygnus X cloud complex and have performed SiO(2-1) follow-up observations of the best candidate progenitors of high-mass stars. Our main findings can be summarized as follows:

1. Our MAMBO-2 (1.2 mm, 11″ resolution) imaging of the Cygnus X molecular cloud complex gives a complete view of the cloud structures ranging from 0.03 to 5 pc, i.e. from dense cores to clumps (cf. the terminology used for nearby

molecular clouds). We performed a multi-resolution analysis to identify a few tens of massive large-scale ($\sim$ 0.7 pc) clumps and extract 129 compact ($\sim$ 0.1 pc) dense cores.

2. The Cygnus X dense cores are the high-density parts of massive clumps which resemble HMPOs or IRDCs. The dense cores have similar sizes ($\sim$ 0.1 pc) but mass and volume-averaged densities ($4 - 950\ M_{\odot}$, $\sim 1.1 \times 10^5$ cm^{-3}) larger than those of nearby, pre-stellar dense cores. The most massive ($> 40\ M_{\odot}$) and thus "extreme-density" cores of this large and unbiased sample are probable precursors of high-mass stars spanning, for the first time, the whole evolution from pre-stellar cores to "embedded H II regions".
3. We have used the *MSX* 21 μm flux arising from our MAMBO-2 dense cores to identify the high-luminosity ($> 10^3\ L_{\odot}$) massive young stellar objects of Cygnus X: 15 UCH II regions and 10 "high-luminosity infrared protostars". Strikingly, half of the dense cores considered as the best candidate precursors of high-mass stars are found to be infrared-quiet (i.e. 17 Cygnus X dense cores more massive than $40\ M_{\odot}$ have $F_{21\mu m} < 10$ Jy).
4. We have surveyed the most massive ($> 40\ M_{\odot}$) dense cores of Cygnus X in SiO(2-1) to search for shocked gas in molecular outflows and/or hot cores. The association of high-velocity SiO emission with *all* massive infrared-quiet cores provides persuasive evidence that stars are already forming in these cores as outflows are tracing the accretion process. The brightness and shape of the SiO line compared to that of nearby, low-mass protostars suggest that these extreme-density cores may host "massive infrared-quiet protostars".
5. Our unbiased survey of the massive young stellar objects in Cygnus X shows that massive infrared-quiet protostars do exist, and that their lifetime should be comparable to that of more evolved high-luminosity infrared protostars. By comparing the number of high-mass protostars and OB stars in the whole of Cygnus X, we estimate a statistical lifetime of 3×10^4 yr for high-mass protostars. One order of magnitude smaller than the lifetime of nearby, low-mass protostars, such a value agrees, within a factor of 3, with the free-fall time of Cygnus X dense cores.
6. Our complete census of massive young stellar objects in Cygnus X fails to discover the high-mass analogs of pre-stellar dense cores ($\sim$ 0.1 pc, $> 10^4$ cm^{-3}). Their corresponding lifetime ($< 10^3$ yr) is smaller than one free-fall time, in marked contrast with nearby, pre-stellar cores that typically live for 2–5 free-fall times. We propose that the starless, massive but lower-density clumps ($800\ M_{\odot}$, $\sim$ 0.8 pc, $\sim 7 \times 10^3$ cm^{-3}) that we observe rapidly concentrate and collapse to form high-mass protostars.
7. Lifetime measurements of the pre-stellar and protostellar phases of high-mass stars in Cygnus X suggest a dynamical contraction for pre-stellar cores and a supersonic evolution for protostars. Highly turbulent processes throughout the Cygnus X molecular cloud complex would be necessary in such a dynamical picture of the high-mass star formation process.
8. Our Cygnus X study suggests that far-infrared to submillimeter continuum imaging of entire star-forming complexes (such as those proposed with *Herschel* by Motte, Zavagno, Bontemps et al.: the HOBYS[7] Key Programme) will definitely contribute to a better knowledge of the high-mass star formation process during its earliest phases.

Acknowledgements. We are grateful to Axel Weiss, Roberto Neri and Clemens Thum for their help in taking and reducing the MAMBO data. We thank Henrik Beuther and Jill Ratherborne for providing electronic versions of their tables, as well as Friedrich Wyrowski for unveiling his Effelsberg results before publication. We are grateful to Tom Megeath for useful discussions on Orion and Arnaud Belloche for the suggestion of using volume-averaged densities.

References

Abergel, A., Bernard, J. P., Boulanger, F., Cesarsky, D., Falgarone, E., et al. 2002, A&A, 389, 239
André, P., Ward-Thompson, D., Barsony, M. 2000, in Protostars & Planets IV, ed. V. Mannings, A. Boss, & S. Russell (Tucson: Univ. Arizona Press), 59
André, P., Belloche, A., Motte, F., Peretto, N. 2007, A&A, in press
Argon, A. L., Reid, M. J., Menten, K. M. 2000, ApJS, 129, 159
Bertoldi, F., McKee, C. F. 1992, ApJ, 395, 140
Beuther, H., Schilke, P., Menten, K. M., Motte, F., Sridharan, T. K., Wyrowski, F. 2002, ApJ, 566, 945
Bonnell, I. A., Bate, M. R., Clarke, C. J., Pringle, J. E. 2001, MNRAS, 323, 794
Bontemps, S., Motte, F., Schneider, N. in prep.
Bontemps, S., André, P., Kaas, A. A., Nordh, L., Olofsson, G., et al. 2001, A&A, 372, 173
Bontemps, S., André, P., Terebey, S., Cabrit, S. 1996, A&A, 311, 858
Braz, M. A., Epchtein, N. 1983, A&AS, 54, 167
Broguière, D., Neri, R., Sievers, A. 1995, NIC bolometer users guide (IRAM internal report)
Bronfman, L., Nyman, L.-A., May, J. 1996, A&AS, 115, 81
Brown, A. G. A., de Geuss, E. J., de Zeeuw, P. T. 1994, A&A, 289, 101
Carey, S. J., Feldman, P. A., Redman, R. O., Egan, M. P., MacLeod, J. M., Price, S. D. 2000, ApJ, 543, L157
Casoli, F., Combes, F., Dupraz, C., Gerin, M., Boulanger, F. 1986, A&A, 169, 281
Chandler, C. J., Gear, W. K., Chini, R. 1993, MNRAS, 260, 337
Chandler, C. J., Moore, T. J. T., Mountain, C. M., Yamashita, T. 1993, MNRAS, 261, 694
Churchwell, E. 1999, in The Origin of Stars and Planetary Systems, ed. C. J. Lada & N. D. Kylafis (Kluwer Academic Publishers), 515
Davis, C. J., Kumar, M. S. N., Sandell, G., Froebrich, D., Smith, M. D., Currie, M. J. 2007, MNRAS, 374, 29
Downes, D., Rinehart, R. 1966, ApJ, 144, 937
Egan, M. P., Price, S. D., Moshir, M. M., Cohen, M., Tedesco, E., Murdock, T. L., Zweil, A., Burdick, S., Bonito, N., Gugliotti, G. M., Duszlak, J. 2001, VizieR On-line Data Catalog, originally published in: Air Force Research Lab. Technical Rep.
Emerson, D. T., Klein, U., Haslam, C. G. T. 1979, A&A, 76, 92
Faúndez, S., Bronfman, L., Garay, G., Chini, R., Nyman, L.-Å., May, J. 2004, A&A, 426, 97
Hanson, M. 2003, ApJ, 597, 957
Harris, S. 1973, MNRAS, 162, Short Communication
Haschick, A. D., Reid, M. J., Burke, B. F., Moran, J. M., Miller, G. 1981, ApJ, 244, 76
Hatchell, J., Fuller, G. A., Millar, T. J. 2001, A&A, 372, 281
Helmich, F. P., van Dishoek, E. F. 1997, A&AS, 124, 205
Henning, T., Michel, B., & Stognienko, R. 1995, Planet. Space Sci. (Special issue: Dust, molecules and backgrounds), 43, 1333
Hill, T., Burton, M. G., Minier, V., Thompson, M. A., Walsh, A. J., Hunt-Cunningham, M., Garay G. 2005, MNRAS, 363, 405
Kenyon, S.J., & Hartmann, L.W. 1995, ApJS, 101, 117
Kirk, J. M., Ward-Thompson, D., André, P. 2005, MNRAS, 360, 1506
Knödlseder, J. 2000, A&A, 360, 539
Kramer, C., Stutzki, J., Rohrig, R., Corneliussen, U. 1998, A&A, 329, 249
Kreysa, E., Gemünd, H. P., Gromke, J., Haslam, C. G., Reichertz, L., Haller, E. E., Beeman, J. W., Hansen, V., Sievers, A., Zylka, R. 1998, in SPIE 3357, Advanced Technology MMW, Radio, and Terahertz Telescopes, ed. T. G. Phillips, 319
Krumholz, M. R., Klein, R. I., McKee, C. F. 2007, ApJ, 656, 959
Kurtz, S., Cesaroni, R., Churchwell, E., Hofner, P., Walmsley, C. M. 2000, in: V. Mannings, A. Boss, & S. Russell (ed.), Protostars & Planets IV, p. 299
Kurtz, S., Churchwell, E., Wood, D. O. S. 1994, ApJS, 91, 659
Leung, H. O., Thaddeus, P. 1992, ApJS, 81, 267
Marston, A. P., Reach, W. T., Noriega-Crespo, A., Rho, J., Smith, H. A., et al. 2004, ApJS, 154, 333
Martín-Pintado, J., Bachiller, R., Fuente, A. 1992, A&A, 254, 315
Minier, V., Conway, J. E., Booth, R. S. 2001, A&A, 369, 278

[7] "HOBYS: the *Herschel* imaging survey of OB Young Stellar objects" is a Guaranteed Time Key Programme jointly proposed by the SPIRE and PACS consortia, and the Herschel Science Centre.

Molinari, S., Brand, J., Cesaroni, R., Palla, F. 2000, A&A, 355, 617
Molinari, S., Testi, L., Brand, J., Cesaroni, R., Palla, F. 1998a, ApJ, 505, L39
Molinari, S., Brand, J., Cesaroni, R., Palla, F., Palumbo, G. G. C. 1998b, A&A, 336, 339
Mookerjea, B., Kramer, C., Nielbock, M., Nyman, L.-Å. 2004, A&A, 426, 119
Motte, F., & André, P. 2001, A&A, 365, 440
Motte, F., Schilke, P., Lis, D. C. 2003, ApJ, 582, 277
Motte, F., André, P., Neri, R. 1998, A&A, 336, 150
Motte, F., Bontemps, S., Schilke, P., Lis, D. C., Schneider, N., Menten, K. M. 2005, in IAU Symp. 227, Massive star birth: A crossroads of Astrophysics, ed. Cesaroni, Felli, Churchwell, & Walmsley, 151
Mueller, K. E., Shirley, Y. L., Evans, N. J., II, Jacobson, H. R. 2002, ApJS, 143, 469
Nisini, B., Codella, C., Giannini, T., Santiago Garcia, J., Richer, J. S., Bachiller, R., Tafalla, M. 2007, A&A, 462, 163
Onishi, T., Mizuno, A., Kawamura, A., Tachihara, K., Fukui, Y. 2002, ApJ, 575, 950
Ossenkopf, V., Henning, T. 1994, A&A, 291, 943
Palla, F. , Brand, J., Cesaroni, R., Comoretto, G., Felli, M. 1991, A&AS, 246, 249
Palla, F., Testi, L., Hunter, T. R., Taylor, G. B., Prusti, T., Felli, M., Natta, A., Stanga, R. M. 1995, A&A, 293, 521
Pestalozzi, M. R.; Minier, V.; Booth, R. S 2005, A&A, 432, 737
Pipher, J. L., Sharpless, S., Savedoff, M. P., Kerridge, S. J., Krassner, J., et al. 1976, A&A, 51, 255
Plume, R., Jaffe, D. T., Evans, N. J., II, Martín-Pintado, J., Gómez-González, J. 1997, ApJ, 476, 730
Rathborne, J. M., Jackson, J. M., Simon, R. 2006, ApJ, 641, 389
Reid, M. A.; Wilson, C. D. 2005, ApJ, 625, 891
Richer, J. S., Padman, R., Ward-Thompson, D., Hills, R. E., Harris, A. I. 1993, MNRAS, 262, 839
Sandell, G., Sievers, A. 2004, ApJ, 600, 269
Schilke, P., Walmsley, C. M., Pineau des Forets, G., Flower, D. R. 1997, A&A, 321, 293
Schneider, N., Bontemps, S., Simon, R., Jakob, R., Motte, F., Miller, M., Kramer, C. 2006, A&A, 458, 855
Schneider, N., Simon, R., Kramer, C., Stutzki, J., Bontemps, S. 2002, A&A, 384, 225
Shepherd, D. S., Kurtz, S. E., Testi, L. 2004, ApJ, 601, 952
Smith, M. D., Eisloffel, J., Davis, C. J. 1998, MNRAS, 297, 687
Sridharan, T. K., Beuther, H., Schilke, P., Menten, K. M., Wyrowski, F. 2002, ApJ, 566, 931
Starck, J.-L., Murtagh, F. 2006, Astronomical image and data analysis, Astronomy and astrophysics library, Berlin: Springer
Stutzki, J., Güsten, R. 1990, ApJ, 356, 513
Teyssier, D., Sievers, A. 1998, IRAM internal report
Thompson, M. A., Gibb, A. G., Hatchell, J. H., Wyrowski, F., Pillai, T. 2005, in: A. Wilson (ed.), The dusty and molecular universe: a prelude to Herschel and ALMA, ESA SP-577, p. 425
Trinidad, M. A., Curiel, S., Cantó, J., D'Alessio, P., Rodríguez, L. F., Torrelles, J. M., Gómez, J. F., Patel, N., Ho, P. T. P. 2003, ApJ, 589, 386
Uyaniker, B., Fürst, E., Reich, W., Aschenbach, B., Wielebinski, R. 2001, A&A, 371, 675
Valdettaro, R., Palla, F., Brand, J., Cesaroni, R., Comoretto, G., Di Franco, S., Felli, M., Natale, E., Palagi, F., Panella, D., Tofani, G. 2001, A&A, 368, 845
Vallée, J. P., Fiege, J. D. 2006, ApJ, 636, 332
van der Tak, F. F. S. 2002, in ASP Conf. Ser. 267, Hot Star Workshop III: The Earliest Phases of Massive Star Birth, ed. P. A. Crowther (San Francisco: ASP), 33
van der Tak, F. F. S., van Dishoeck, E. F., Evans, N. J., II, Bakker, E. J., Blake, G. A. 1999, ApJ, 522, 991
Vázquez-Semadeni, E., Kim, J.. Shadmehri, M., Ballesteros-Paredes, J. 2005, ApJ, 618, 344
Ward-Thompson, D., Motte, F., André, P. 1999, MNRAS, 305, 143
Wendker, H. J., Higgs, L. A., Landecker, T. L. 1991, A&A, 241, 551
Williams,, S. J., Blitz, L., McKee, C. F. 2000, in Protostars & Planets IV, ed. V. Mannings, A. Boss, & S. Russell (Tucson: Univ. Arizona Press), 97
Wood, D. O. S., Churchwell, E. 1989, ApJ, 340, 265
Yorke, H. W., Sonnhalter, C. 2002, ApJ, 569, 846
Ziurys, L. M., & Friberg, P. 1987, ApJ, 314, L49
Zoonematkermani, S., Helfand, D. J., Becker, R. H., White, R. L., Perley, R. A. 1990, ApJS, 74, 181
Zylka, R. 1998, Pocket Cookbook for the MOPSI software

Online Material

Appendix A: A skynoise reduction technique dedicated to extended sources

Ground-based (sub)millimeter continuum observations of astronomical sources are hampered by the emission of the atmosphere and its fluctuations, called "skynoise". The bulk of the atmospheric emission and its slow variations in time can be removed by the dual-beam scanning mode generally used for bolometer observations (the "EKH method", Emerson et al. 1979). However, the residual atmospheric fluctuations generate an excess noise in the restored maps that can dominate the Gaussian noise (see e.g. Fig. 10a). In the present study, more than half of the on-the-fly maps were observed with a skynoise level qualified as medium or high. In our maps, medium skynoise implies $\sigma = 30-60$ mJy beam^{-1} and high skynoise $\sigma > 60$ mJy beam^{-1}, while the nominal rms is $\sigma \sim 15$ mJy beam^{-1}. This excess noise can theoretically be suppressed by using the fact that it is well correlated across the whole array. Several skynoise reduction algorithms have been developed assuming that either the atmospheric emission is equal in all receivers at all times ("mean" or "neighbor" approximation), or that it is correlated on a few seconds of time with correlation coefficients decreasing when the angular separation of receivers increases (see e.g. NIC and MOPSIC IRAM softwares for bolometer-array data, Broguière et al. 1995 and Zylka 1998). While efficient for the detection of pointlike sources, such assumptions can have dramatic consequences on the representation of the extended emission. Indeed, the large-scale structure of a source leads to a correlation of bolometer signals which is non-zero, and caution must be taken not to filter out most of the extended emission.

We have developed a program which uses a source model and the mean approximation to remove the skynoise while preserving, as much as possible, the structure of sources like molecular clouds (compare Figs. 10a-b). We describe below its four steps:

(1) The first step consists of creating a good source model. A first-order data processing is done by reducing all individual maps and combining them with weights consistent with their intrinsic quality, i.e. accounting for both Gaussian noise and skynoise levels (see e.g. Fig. 10a). This first-order mosaic is used as a model of the source after cutting its noisier parts (mostly map edges) and removing artefacts such as negative levels stronger than the rms.

(2) This source model is then subtracted from all the original scans. To do so, we first simulate the on-the-fly dual-beam signals of each bolometer when the MAMBO-2 camera is mapping the source model with the observational geometry of the real scans (see Motte & André 2001, and the routine "simulate" in NIC). These simulated source signals are then removed from the original on-the-fly dual-beam signals recorded by each bolometer. At this point, and for each scan, the bolometer data streams should only contain Gaussian noise and skynoise.

(3) As a third step, the skynoise emission contained in each processed scan is estimated by using the averaging method. While cruder than any "correlation method" (like that proposed in NIC), it allows the treatment of each observing point (taken every half a second) independently. We often find the averaging method to be more efficient, suggesting that the skynoise power is strong at high frequency.

(4) Afterwards, the original scans are reduced for skynoise by subtracting, for each scan, the skynoise data stream estimated above from the on-the-fly dual-beam signals of each bolometer. Finally, the individual scans, now treated for skynoise, are reduced with the default procedure and combined to create a better (second-order processed) mosaic (see e.g. Fig. 10b).

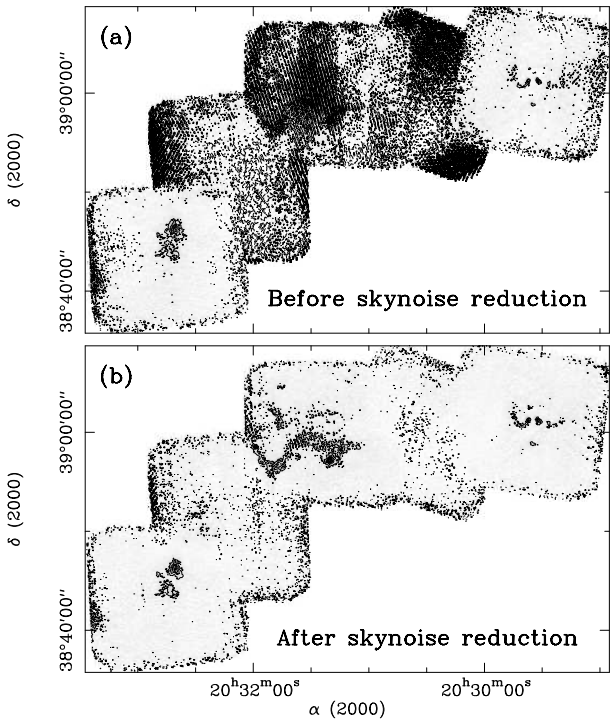

Fig. 10. 1.2 mm map of the DR13 filament in the Cygnus X molecular cloud complex obtained with MAMBO-2 at the IRAM 30 m telescope. Contour levels are -45 mJy beam^{-1}and then 45 to 315 mJy beam^{-1} with steps of 45 mJy beam^{-1}. **(a)** Mosaic built from individual maps taken with low to medium skynoise. As a result, the rms noise level ranges from 15 mJy beam^{-1} to 60 mJy beam^{-1}. **(b)** Mosaic built from individual maps processed by our skynoise reduction program. The resulting noise level is relatively uniform with $\sigma = (14 \pm 2)$ mJy beam^{-1}.

This process can evidently be iterated to improve the map sensitivity but a single iteration already reduces most of the skynoise and probably gives more secure results. The final individual maps have a noise rms of 20 ± 5 mJy beam^{-1}, 15 mJy beam^{-1} being the nominal rms in the absence of skynoise, and with a zenith atmospheric opacity of ~ 0.2. Our skynoise reduction technique has thus improved the map sensitivity by a factor of ~ 2 on average, and up to a factor of 6 for the poorer quality original maps.

Our method relies on the quality of the source model and thus mainly on the redundancy of observations taken in every single pixel. The redundancy is currently ~ 20 for one single map and ~ 40 on average, since most parts were imaged several times. The mosaics shown in Figs. 2a-c recover most of the extended emission up to $\sim 10'$, which is the azimuthal size of individual maps. In agreement, the Cygnus X main region has recently been imaged with the SHARC-II camera installed at the CSO telescope (Motte et al. in prep.). Those data generally confirm the cloud structures detected in our MAMBO-2 maps. We acknowledge, however, that the extended emission is attenuated in a couple of sites where data are too noisy and not redundant enough to build a good source model (e.g. south of DR23).

Appendix B: An extraction technique dedicated to compact sources

Since stars are generally forming in the densest parts of molecular clouds, we have developed a source extraction technique aiming at identifying and extracting dense compact fragments that should be the best potential sites of star formation.

In spirit, this method is equivalent to an eye search of local density peaks followed by flux measurements with an aperture optimized for each source. We outline below the procedure for this automated method, which was originally developed by Motte et al. (2003):

(1) As a first step, one has to determine the cutoff lengthscale at which the sources of interest (here dense cores, cf. Fig. 11b) separate from their surrounding (here clumps and clouds, cf. Fig. 11c). This scale corresponds to twice the mean outer radius of the most compact objects one can distinguish on the MAMBO-2 map or the mean projected distance between them. This scale is typically about 5 to 10 times the *HPBW*.

(2) For further analysis, we only keep spatial scales smaller than the cutoff lengthscale determined at step 1 (here 1 pc). For this purpose, we use a multiresolution program based on wavelet transforms (MRE, cf. Starck & Murtagh 2006). This makes a series of filtering operations and provides "views" of the image at different spatial scales. We therefore sum[8] all wavelet planes of the original image up to that scale to create images like that shown in Fig. 11b.

(3) As a third step, we use a version of the Gaussclumps program (Stutzki & Güsten 1990; Kramer et al. 1998) which has been customized for continuum images (see Motte et al. 2003 and Mookerjea et al. 2004) and optimized for compact sources[9]. Gaussclumps is applied to the filtered image created at step 2. It identifies compact fragments above a 5 σ level (here 75 mJy beam^{-1}) and gives first-guess parameters of a 2D-Gaussian fit. If the Gaussian shape is not ideally fitting compact fragments, it gives appropriate estimates of their size and mass even when their environment is not perfectly filtered out. Gaussclumps is known to be efficient at deblending compact sources. Noisy edges that usually pose problems (see e.g. Kramer et al. 1998) have been removed.

(4) Finally, the most critical and time consuming step is to improve the extraction of individual fragments from their surrounding background. The main goal is to avoid Gaussian fits being biased to a single lengthscale, which would be that determined at step 1. We therefore repeat steps 2 and 3 for the sources identified at step 3 and use a cutoff scale optimized for each fragment. We estimate the scale up to which one fragment is resolved from its surrounding to be twice the first-guess measure of its Gaussian *FWHM* (see step 3). Therefore, for each of the (here 129) sources, we create a final-guess filtered image and adjust its Gaussian fit parameters.

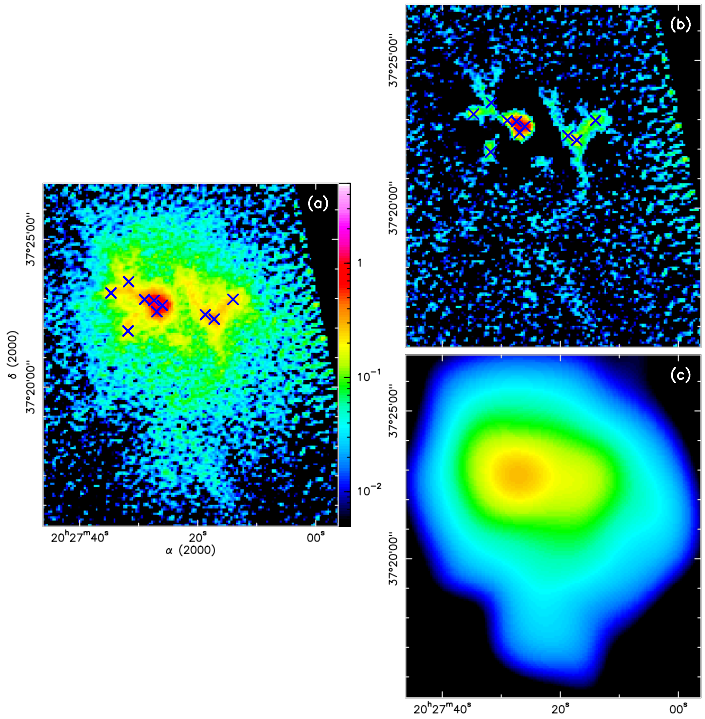

Fig. 11. Separation of cloud structures from the MAMBO-2 map of S106 shown in (**a**) into (**b**) dense cores (i.e. compact structures with size scales smaller than 128″) and (**c**) their environment (i.e. cloud structure with a typical scale > 128″). Dense cores extracted by the technique described in Appendix B are indicated by crosses.

[8] The original image can be expressed as the sum of all wavelet views (also called planes) plus the smoothed image (last plane containing all remaining scales).

[9] Gaussclumps parameters for initial guesses are: *FWHM*= 1.1 × *HPBW*, aperture = 1.5 × *HPBW*

Table 1. Properties of dense cores (compact cloud fragments) detected in the Cygnus X complex

	Fragment name	$S^{peak}_{1.2\,mm}$ [a] (mJy/beam)	$FWHM$ [a] (pc × pc)	$S^{int}_{1.2\,mm}$ [a] (mJy)	$M_{1.2\,mm}$ [b] ($M_\odot$)	$< n_{H_2} >$ [c] (cm^{-3})	MSX[d] 21 μm (Jy)	Name, comments, and coincidence with stellar activity signatures
	CygX-North region							
N1	J203532.7+421953	120	0.15 × 0.09	320	17	4.7×10^4	–	
N2	J203534.0+422023	110	0.22 × 0.07	380	20	4.0×10^4	3.74	MSX 81.3039+1.0520
N3	J203534.2+422005	720	0.11 × 0.09	1580	84	3.6×10^5	–	
N4	J203558.0+422431	90	0.06 × 0.06	120	< 6	$< 1.2 \times 10^5$	–	probably not an embedded YSO[e]
N5	J203606.5+413958	160	0.12 × 0.07	350	19	9.4×10^4	–	
N6	J203608.1+413958	260	0.23 × 0.14	1280	44-68	$3.2\text{-}5.0\times10^4$	90.88	IRAS 20343+4129
N7	J203615.7+425305	80	0.12 × 0.10	190	10	3.2×10^4	–	
N8	J203638.4+422911	170	0.17 × 0.09	500	27	6.4×10^4	Abs	
N9	J203639.5+425113	100	0.23 × 0.14	500	26	1.7×10^4	Abs	
N10	J203652.2+413623	590	0.14 × 0.09	1530	<52-81	$<1.5\text{-}2.4\times10^5$	99.33	IRAS 20350+4126, cm[1] free-free, maser[2] (CH_3OH/OH)
N11	J203656.8+421320	180	0.11 × 0.06	340	18	1.4×10^5	Abs	
N12	J203657.4+421127	740	0.11 × 0.09	1630	86	3.8×10^5	Abs	
N13	J203658.4+421118	90	0.04 × 0.03	100	5	7.1×10^5	Abs	
N14	J203700.9+413457	500	0.10 × 0.07	940	50	3.5×10^5	19.71	IRAS 20352+4124
N15	J203710.9+413339	80	0.09 × 0.03	110	6	2.1×10^5	–	
N16	J203716.9+421631	210	0.12 × 0.12	550	29	7.5×10^4	3.87	MSX 81.4452+0.7635
N17	J203726.5+413319	100	0.15 × 0.03	200	10	1.6×10^5	–	
N18	J203730.2+421359	110	0.17 × 0.13	430	23	2.7×10^4	–	
N19	J203745.8+424343	80	0.09 × 0.03	110	6	1.9×10^5	–	
N20	J203747.4+423842	100	0.10 × 0.03	150	8	2.1×10^5	2.06	MSX 81.7947+0.9116
N21	J203801.7+423933	100	0.16 × 0.14	380	20	2.5×10^4	–	
N22	J203803.4+423956	90	0.27 × 0.11	420	22	1.9×10^4	–	
N23	J203804.9+423317	80	0.22 × 0.06	250	13	4.0×10^4	–	
N24	J203805.8+423952	140	0.17 × 0.17	650	34	3.0×10^4	–	
N25	J203810.4+423805	170	0.12 × 0.11	450	24	6.5×10^4	–	
N26	J203821.2+421131	100	0.20 × 0.10	340	18	2.6×10^4	–	
N27	J203831.6+423804	90	0.10 × 0.10	200	11	4.1×10^4	–	
N28	J203833.7+423944	140	0.19 × 0.11	510	27	3.9×10^4	–	
N29	J203834.6+420619	110	0.25 × 0.13	540	29	2.0×10^4	–	
N30	J203836.6+423730	3650	0.15 × 0.10	10640	<361-563	$<0.8\text{-}1.2\times10^6$	136	W75N(B), cm free-free[3], maser[4] (CH_3OH/H_2O/OH)
N31	J203836.9+423750	120	0.03 × 0.03	130	7	1.2×10^6	–	close to H II region W75N(A)
N32	J203838.3+423733	540	0.16 × 0.10	1630	86	1.7×10^5	–	
N33	J203847.0+423800	100	0.08 × 0.07	170	9	8.1×10^4	–	
N34	J203854.3+421917	150	0.19 × 0.07	430	23	6.1×10^4	–	
N35	J203854.4+421855	90	0.13 × 0.03	160	8	1.5×10^5	–	
N36	J203858.5+422330	90	0.19 × 0.03	210	11	1.2×10^5	–	
N37	J203858.6+422435	80	0.03 × 0.03	80	4	8.7×10^5	–	
N38	J203859.4+422223	830	0.18 × 0.09	2610	138	2.7×10^5	–	DR21(OH)-W
N39	J203859.9+422732	70	0.16 × 0.08	200	10	3.0×10^4	–	
N40	J203859.8+422343	400	0.33 × 0.08	2000	106	1.1×10^5	–	DR21(OH)-N2
N41	J203900.2+422325	180	0.03 × 0.03	180	10	1.9×10^6	–	DR21(OH)-N1
N42	J203900.3+421907	90	0.05 × 0.03	100	5	4.5×10^5	–	
N43	J203900.6+422435	370	0.19 × 0.10	1250	66	1.1×10^5	15.9	W75S-FIR1, maser[5,6] (H_2O/OH)
N44	J203901.0+422246	2970	0.14 × 0.11	8430	446	1.0×10^6	6.78	DR21(OH), maser[2,6] (CH_3OH/H_2O/OH)
N45	J203901.1+421814	130	0.13 × 0.08	300	16	6.4×10^4	Abs	
N46	J203901.4+421934	4200	0.19 × 0.14	17930	<609-949	$<5.9\text{-}9.1\times10^5$	272	DR21, cm[7] free-free, maser[8] (H_2O)
N47	J203901.4+421954	630	0.08 × 0.03	840	<28-44	$<1.2\text{-}1.9\times10^6$	272	DR21-D, cm[7] free-free
N48	J203901.5+422203	1160	0.17 × 0.11	3720	197	3.5×10^5	–	DR21(OH)-S
N49	J203902.0+422700	80	0.15 × 0.03	160	8	1.2×10^5	–	
N50	J203901.9+421835	80	0.24 × 0.03	240	12	1.0×10^5	–	
N51	J203902.4+422459	680	0.19 × 0.10	2370	125	2.0×10^5	26.50	W75S-FIR2
N52	J203903.0+422615	180	0.16 × 0.12	630	33	4.9×10^4	–	
N53	J203903.2+422549	590	0.14 × 0.09	1600	85	2.2×10^5	–	maser[2] (CH_3OH/H_2O)
N54	J203903.6+422530	150	0.18 × 0.08	450	24	6.0×10^4	10.85	W75S-FIR3
N55	J203906.1+421819	100	0.15 × 0.05	220	11	8.0×10^4	Abs	
N56	J203916.9+421607	270	0.12 × 0.08	600	32	1.4×10^5	3.68	MSX 81.6632+0.4651
N57	J203919.3+421556	130	0.09 × 0.05	210	11	1.5×10^5	Abs	ERO1

Table 1. Continued

	Fragment name	$S^{peak}_{1.2\,mm}$ [a] (mJy/beam)	$FWHM$ [a] (pc × pc)	$S^{int}_{1.2\,mm}$ [a] (mJy)	$M_{1.2\,mm}$ [b] ($M_\odot$)	$< n_{H_2} >$ [c] (cm^{-3})	MSX[d] 21 μm (Jy)	Name, comments, and coincidence with stellar activity signatures
N58	J203925.9+412001	430	0.23 × 0.19	2730	<92-144	<4.2-6.6×10^4	634.13	IRAS 20375+4109, cm[9] free-free
N59	J203931.2+412003	200	0.12 × 0.05	370	20	2.0 × 10^5	–	
N60	J203936.2+411937	160	0.16 × 0.13	560	30	4.2 × 10^4	–	
N61	J203957.6+415911	100	0.12 × 0.09	230	12	4.7 × 10^4	11.63	MSX 81.5168+0.1926
N62	J204003.6+412756	140	0.18 × 0.12	500	27	3.6 × 10^4	–	close to MSX 81.1109-0.1459 and MSX 81.1225-0.1343
N63	J204005.2+413213	740	0.08 × 0.05	1090	58	1.1 × 10^6	Abs	
N64	J204027.2+415651	100	0.12 × 0.09	220	12	4.6 × 10^4	Abs	
N65	J204028.4+415711	230	0.16 × 0.12	780	41	6.4 × 10^4	2.0	
N66	J204029.8+414933	110	0.15 × 0.06	250	13	6.1 × 10^4	Abs	
N67	J204031.0+414957	100	0.08 × 0.05	150	8	1.4 × 10^5	Abs	
N68	J204033.5+415903	390	0.10 × 0.10	840	44	2.0 × 10^5	Abs	
N69	J204033.7+415059	110	0.47 × 0.18	1280	68	1.2 × 10^4	–	
N70	J204034.3+413845	80	0.12 × 0.07	170	9	5.0 × 10^4	Abs	
N71	J204038.2+415259	80	0.21 × 0.06	230	12	3.4 × 10^4	–	
N72	J204045.7+415750	100	0.28 × 0.13	540	29	1.7 × 10^4	–	
	CygX-South region							
S1	J201643.3+392313	90	0.08 × 0.05	140	8	1.1 × 10^5	3.08	IRAS 20149+3913
S2	J201648.5+392212	100	0.17 × 0.06	260	14	5.4 × 10^4	Abs	
S3	J201658.6+392106	210	0.12 × 0.08	440	23	1.2 × 10^5	5.27	IRAS 20151+3911
S4	J201737.0+392139	90	0.14 × 0.10	230	12	3.1 × 10^4	Abs	
S5	J201745.3+392041	120	0.16 × 0.09	340	18	4.1 × 10^4	–	
S6	J202036.5+393821	120	0.03 × 0.03	120	6	1.2 × 10^6	–	
S7	J202038.0+393820	280	0.22 × 0.03	760	40	3.5 × 10^5	–	
S8	J202038.8+393751	900	0.19 × 0.12	3540	<121-188	<1.4-2.1×10^5	145.48	Mol121S, cm[10] free-free, maser[11] (H_2O)
S9	J202039.5+393738	120	0.03 × 0.03	130	7	1.1 × 10^6	–	
S10	J202044.4+393520	180	0.19 × 0.14	760	40	4.1 × 10^4	–	
S11	J202153.7+395933	110	0.15 × 0.11	340	18	3.6 × 10^4	–	
S12	J202220.1+395821	130	0.16 × 0.08	350	18	5.5 × 10^4	–	close to IRAS 20205+3948
S13	J202632.4+395721	160	0.15 × 0.11	500	27	5.0 × 10^4	4.84	MSX 78.3762+1.0191
S14	J202634.8+395725	200	0.09 × 0.05	330	17	2.4 × 10^5	Abs	
S15	J202714.0+372258	120	0.29 × 0.12	630	34	2.2 × 10^4	Abs	
S16	J202717.2+372218	260	0.11 × 0.05	460	24	3.0 × 10^5	–	
S17	J202718.7+372227	130	0.07 × 0.06	210	11	1.4 × 10^5	–	
S18	J202726.0+372246	960	0.21 × 0.13	4270	<145-226	<1.2-2.0×10^5	413.63	S106-IR, cm[12] free-free, maser[8] (H_2O)
S19	J202726.9+372233	310	0.08 × 0.03	420	<14-22	<6.1-9.5×10^5	413.63	part of S106-IR, cm[12] free-free
S20	J202727.4+372256	510	0.11 × 0.11	1300	<44-69	<1.2-2.0×10^5	413.63	part of S106-IR, cm[1] free-free
S21	J202729.0+372258	120	0.03 × 0.03	130	7	1.2 × 10^6	–	
S22	J202731.7+372334	80	0.13 × 0.03	150	8	1.5 × 10^5	–	
S23	J202731.8+372154	110	0.24 × 0.03	310	16	1.2 × 10^5	–	
S24	J202734.7+372311	140	0.18 × 0.09	420	22	4.9 × 10^4	–	
S25	J202923.6+401110	120	0.05 × 0.03	140	7	6.1 × 10^5	–	
S26	J202924.8+401118	880	0.14 × 0.10	2340	<80-124	<2.1-3.4×10^5	1023.40	AFGL 2591, cm[13] free-free, maser[8] (H_2O/OH?)
S27	J202931.8+390113	130	0.19 × 0.09	420	<14-22	<2.7-4.2×10^4	23.55	MSX 77.9550+0.0058, cm[9] free-free
S28	J202936.8+390112	120	0.12 × 0.08	270	< 9 – 14	< 3.6 – 5.6 × 10^4	204.20	IRAS 20277+3851, cm[1] free-free
S29	J202958.3+401558	160	0.23 × 0.12	710	37	3.4 × 10^4	–	
S30	J203112.6+400316	360	0.16 × 0.16	1560	82	7.7 × 10^4	–	close to IRAS 20293+3952
S31	J203114.2+400305	110	0.13 × 0.07	220	12	6.5 × 10^4	–	
S32	J203120.3+385716	250	0.21 × 0.11	1010	54	6.0 × 10^4	–	
S33	J203144.5+385639	80	0.14 × 0.11	230	12	2.7 × 10^4	–	
S34	J203157.8+401830	150	0.20 × 0.12	610	32	3.4 × 10^4	–	in IRDC G79.3-P3
S35	J203158.8+385836	200	0.12 × 0.06	410	22	1.4 × 10^5	5.00	
S36	J203220.8+401949	80	0.07 × 0.03	100	5	2.5 × 10^5	–	in IRDC G79.34+0.33
S37	J203222.0+402012	240	0.18 × 0.12	860	45	6.4 × 10^4	4.44	IRAS 20305+4010 in IRDC G79.34+0.33
S38	J203222.4+401919	90	0.23 × 0.12	410	22	2.0 × 10^4	–	in IRDC G79.34+0.33
S39	J203229.0+401600	170	0.14 × 0.09	440	<15-23	<4.2-6.6×10^4	37.71	MSX 79.2963+0.2835, cm[1] free-free
S40	J203232.2+401625	80	0.16 × 0.10	240	<8-13	<1.6-2.6×10^4	73.03	MSX 79.3070+0.2768, cm[9] free-free

Table 1. Continued

	Fragment name	$S^{peak}_{1.2\,mm}$ [a] (mJy/beam)	*FWHM* [a] (pc × pc)	$S^{int}_{1.2\,mm}$ [a] (mJy)	$M_{1.2\,mm}$ [b] ($M_\odot$)	$< n_{H_2} >$ [c] (cm^{-3})	MSX[d] 21 μm (Jy)	Name, comments, and coincidence with stellar activity signatures
S41	J203233.9+401653	220	0.19 × 0.11	800	27-42	3.7-5.9×10^4	49.4	part of IRAS 20306+4005
S42	J203239.9+384603	90	0.18 × 0.13	340	18	2.0 × 10^4	–	
S43	J203240.8+384631	140	0.23 × 0.13	650	35	2.9 × 10^4	Abs	
	CygX-NW region							
NW1	J201938.8+405638	280	0.17 × 0.15	1110	<38-59	<4.2-6.6×10^4	400.66	IRAS 20178+4046, cm[1] free-free
NW2	J201940.5+405704	200	0.23 × 0.07	680	36	7.7 × 10^4	–	
NW3	J202029.9+412144	80	0.15 × 0.07	190	10	4.2 × 10^4	–	
NW4	J202030.0+412207	130	0.07 × 0.05	180	10	2.2 × 10^5	–	
NW5	J202030.7+412125	420	0.07 × 0.06	640	22-34	3.2-5.0×10^5	85.85	EM* LkHA 225S, maser[14] (H_2O)
NW6	J202032.1+412354	130	0.15 × 0.03	250	13	2.0 × 10^5	–	
NW7	J202032.2+412123	80	0.07 × 0.03	100	6	2.5 × 10^5	–	
NW8	J202323.0+411749	90	0.10 × 0.04	150	8	1.2 × 10^5	–	
NW9	J202324.0+411739	230	0.10 × 0.04	370	19	3.0 × 10^5	27.47	IRAS 20216+4107
NW10	J202343.6+411657	160	0.20 × 0.08	520	27	5.7 × 10^4	–	
NW11	J202413.0+411700	110	0.13 × 0.09	290	15	4.7 × 10^4	–	
NW12	J202414.3+421143	140	0.06 × 0.06	200	11	2.1 × 10^5	Abs	
NW13	J202419.5+421545	100	0.17 × 0.09	290	15	3.5 × 10^4	–	
NW14	J202431.7+420423	420	0.12 × 0.09	940	32-50	1.2-2.0×10^5	15.58	Mol124 = IRAS 20227+4154, maser[11] (H_2O)

Notes:

(a) Peak flux, deconvolved *FWHM* size, and integrated flux derived from a 2D-Gaussian fit to the 1.2 mm map after background subtraction (cf. Sect. 3.2 and Appendix B). An upper limit *FWHM* of 0.03 pc was assumed for unresolved fragments.

(b) Mass derived from Col. 5 using Eq. (1) and assuming $\kappa_{1.2\,mm}$ = 0.01 $cm^2\,g^{-1}$ and T_{dust} = 20 K. A second estimate with T_{dust} = 40 K is made for H II regions and the brightest infrared protostars of Cygnus X.

(c) Volume-averaged density derived from Col. 4 and Col. 6 using Eq. (2).

(d) The 21 μm fluxes are those given in the *MSX* point source catalog (MSX C6), except for CygX-N30, N43, N46, N47, N65 and S41, for which an aperture flux is measured on the MSX map. The MSX flux of two extended H II regions is equally distributed between CygX-N46 and N47, and between CygX-S18, S19, S20. All fragments detected at 21 μm are also detected at 8 μm with the exception of CygX-N30, N46, N47, and N65. "Abs" means that sources are seen in absorption at 8 μm.

(e) Observations of high-density tracers toward CygX-N4 suggest that this 1.2 mm source does not correspond to a dense cloud fragment. Its nature is yet unclear but it is probably not a site for future or ongoing star formation.

References: (1) Kurtz et al. 1994; (2) Pestalozzi et al. 2005; (3) Haschick et al. 1981; (4) Minier et al. 2001; (5) Argon et al. 2000; (6) Harris 1973; (8) Braz & Epchtein 1983; (9) Zoonematkermani et al. 1990; (10) Molinari et al. 1998b; (11) Palla et al. 1991; (12) Pipher et al. 1976; (13) Trinidad et al. 2003; (14) Palla et al. 1995.

Table 2. Properties of clumps (large-scale cloud structures) detected in the Cygnus X complex

	Structure name	$FWHM$ [a] (pc × pc)	$S^{\rm int}_{1.2\,\rm mm}$ [a] (mJy)	$M_{1.2\,\rm mm}$ [b] ($M_\odot$)	$< n_{\rm H_2} >$ [c] (cm^{-3})	Comments
	CygX-North region					
Cl-N1	J203534.1+422004	0.48 × 0.31	8470	665	5.0×10^4	contains CygX-N1, N2, N3
Cl-N2	J203605.0+420851	1.46 × 0.94	15150	1189	3.1×10^3	Starless?
Cl-N3	J203607.3+414001	0.64 × 0.38	7010	550	1.9×10^4	contains CygX-N5, N6
Cl-N4	J203651.5+413625	0.66 × 0.65	14780	1161	1.7×10^4	contains CygX-N10
Cl-N5	J203657.9+421132	0.58 × 0.49	11690	917	2.5×10^4	contains CygX-N12, N13
Cl-N6	J203701.9+413453	0.81 × 0.64	13580	1066	1.2×10^4	contains CygX-N14
Cl-N7	J203711.9+413338	1.45 × 0.90	16370	1285	3.6×10^3	contains CygX-N15
Cl-N8	J203728.4+421630	1.80 × 1.01	17060	1339	2.3×10^3	
Cl-N9	J203729.8+421409	1.32 × 0.73	14350	1127	4.9×10^3	contains CygX-N18
Cl-N10	J203805.3+423937	0.87 × 0.51	10000	785	1.1×10^4	Starless? contains CygX-N21, N22, N24
Cl-N11	J203833.2+420619	1.25 × 0.74	14880	1168	5.5×10^3	Starless? contains CygX-N29
Cl-N12	J203836.3+423937	1.30 × 0.56	10240	804	5.5×10^3	contains CygX-N28
Cl-N13	J203836.8+423734	0.48 × 0.40	46930	3684	1.9×10^5	contains CygX-N30, N31, N32
Cl-N14	J203900.5+422238	0.88 × 0.44	92460	7259	1.3×10^5	contains CygX-N36, N38, N41, N44, N48
Cl-N15	J203901.3+421935	0.56 × 0.39	70210	5513	2.3×10^5	contains CygX-N42, N46, N47
Cl-N16	J203901.7+422507	0.91 × 0.60	47360	3718	3.8×10^4	contains CygX-N37, N43, N51, N53, N54
Cl-N17	J203927.2+412009	0.78 × 0.59	15980	1254	1.7×10^4	contains CygX-N58, N59
Cl-N18	J203936.4+412001	0.91 × 0.36	5710	449	1.0×10^4	Starless? contains CygX-N60
Cl-N19	J203955.4+420020	1.79 × 1.10	18110	1422	2.2×10^3	contains CygX-N61
Cl-N20	J204003.6+412814	1.03 × 0.77	14080	1105	6.6×10^3	contains CygX-N62
Cl-N21	J204005.1+413210	0.31 × 0.20	3350	263	7.0×10^4	contains CygX-N63
Cl-N22	J204027.8+415707	0.68 × 0.37	5200	408	1.4×10^4	contains CygX-N64, N65
Cl-N23	J204033.3+415045	0.80 × 0.57	8700	683	9.4×10^3	Starless? contains CygX-N67, N69
	CygX-South region					
Cl-S1	J202038.5+393753	0.51 × 0.34	13920	1093	6.3×10^4	contains CygX-S6, S7, S8, S9
Cl-S2	J202044.8+393525	0.67 × 0.45	4870	382	9.4×10^3	contains CygX-S10
Cl-S3	J202716.1+372231	1.23 × 0.69	26640	2092	1.1×10^4	contains CygX-S15, S16, S17
Cl-S4	J202726.9+372248	0.73 × 0.53	33420	2624	4.6×10^4	contains CygX-S18, S19, S20, S21
Cl-S5	J202924.9+401116	0.42 × 0.38	10090	792	5.2×10^4	contains CygX-S25, S26
Cl-S6	J202959.4+401555	1.25 × 0.60	11560	908	5.9×10^3	Starless? contains CygX-S29
Cl-S7	J203112.1+400314	0.62 × 0.49	10710	841	2.1×10^4	contains CygX-S30, S31
Cl-S8	J203119.2+385731	0.86 × 0.56	8740	686	8.6×10^3	contains CygX-S32
Cl-S9	J203156.7+401833	1.39 × 0.60	12140	953	5.2×10^3	Starless? IRDC G79.33P3, contains CygX-S34
Cl-S10	J203221.9+401955	0.92 × 0.79	17490	1373	9.3×10^3	contains CygX-S36, S37, S38
Cl-S11	J203232.3+401635	0.99 × 0.67	14010	1100	8.5×10^3	contains CygX-S39, S40, S41
Cl-S12	J203240.7+384614	0.67 × 0.52	6480	509	1.0×10^4	Starless? contains CygX-S42, S43
	CygX-NW region					
Cl-NW1	J201939.0+405651	0.73 × 0.64	14190	1114	1.5×10^4	contains CygX-NW1, NW2
Cl-NW2	J202030.5+412132	0.64 × 0.41	6890	541	1.7×10^4	contains CygX-NW3, NW4, NW5, NW7
Cl-NW3	J202344.5+411701	0.97 × 0.71	11480	901	6.5×10^3	Starless?, contains CygX-NW10
Cl-NW4	J202420.3+421527	0.96 × 0.66	8160	640	5.3×10^3	Starless?, contains CygX-NW13
Cl-NW5	J202431.7+420419	0.73 × 0.60	8670	681	9.8×10^3	contains CygX-NW14

Notes:

(a) Deconvolved $FWHM$ size and integrated flux derived from a 2D-Gaussian fit to the 1.2 mm map smoothed to a 55″ beam.
(b) Mass derived from Col. 4 using Eq. (1) and assuming $\kappa_{1.2\,\rm mm} = 0.01$ cm^2 g^{-1} and $T_{\rm dust} = 15$ K.
(c) Volume-averaged density derived from Col. 3 and Col. 5 using Eq. (2).

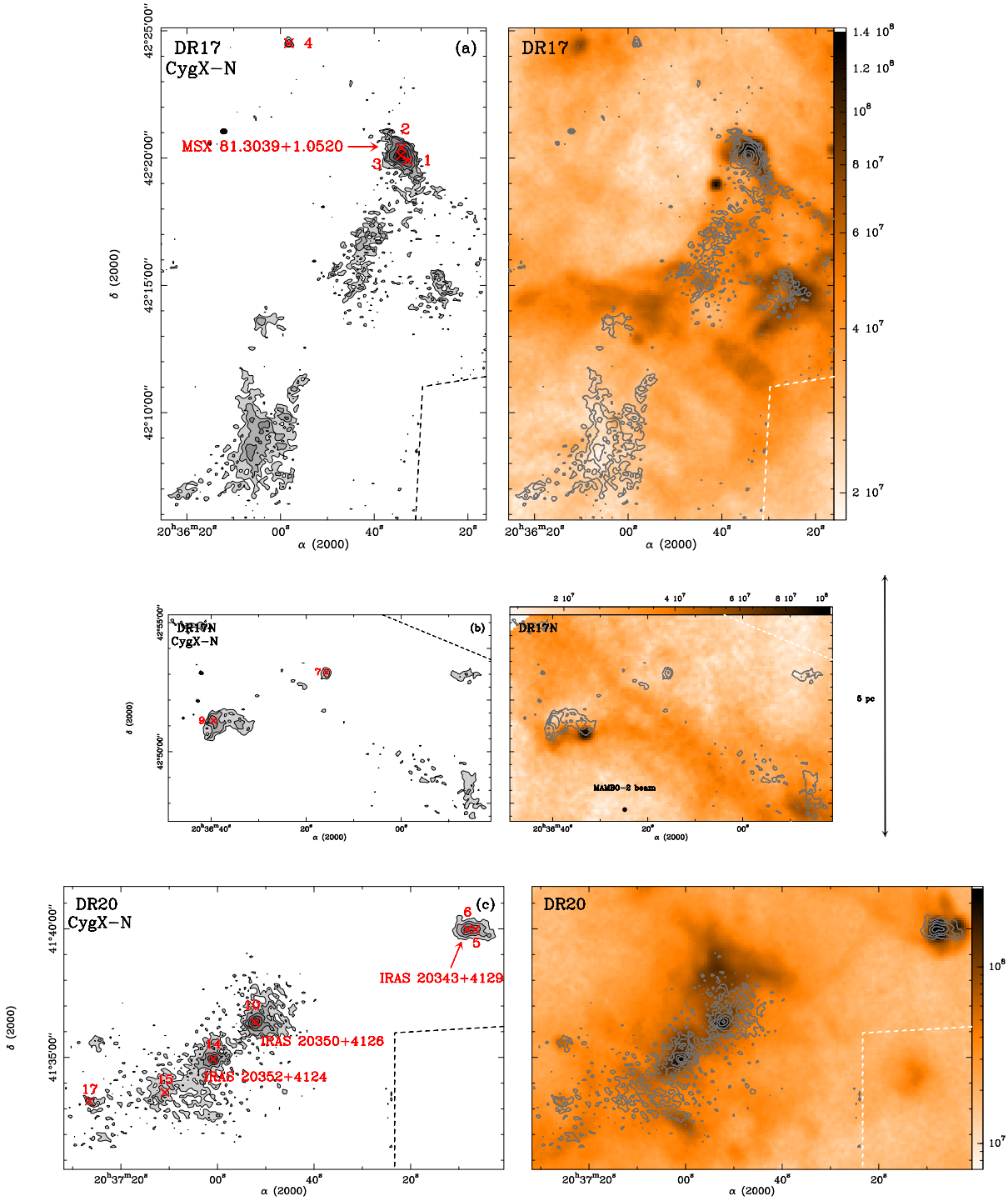

Fig. 12. MAMBO maps of CygX-North (**left**: gray-scale and contours, **right**: contours overlaid on 8 μm images obtained by *MSX* and converted to Jy sr^{-1}) extracted from Fig. 2a. Regions shown are south and north of DR17 (**a–b**) and around DR20 (**c**). The 1.2 mm and 8 μm images have 11″ and 20″ angular resolutions, respectively. The compact cloud fragments discovered in MAMBO images (see Table 1) are labeled and marked by crosses in the gray-scale plot. The infrared sources which coincide with a MAMBO cloud fragment are also indicated. Contour levels are logarithmic and go from 40 to 800 mJy beam^{-1} in **a** and **b**, and from 75 to 800 mJy beam^{-1} in **c**.

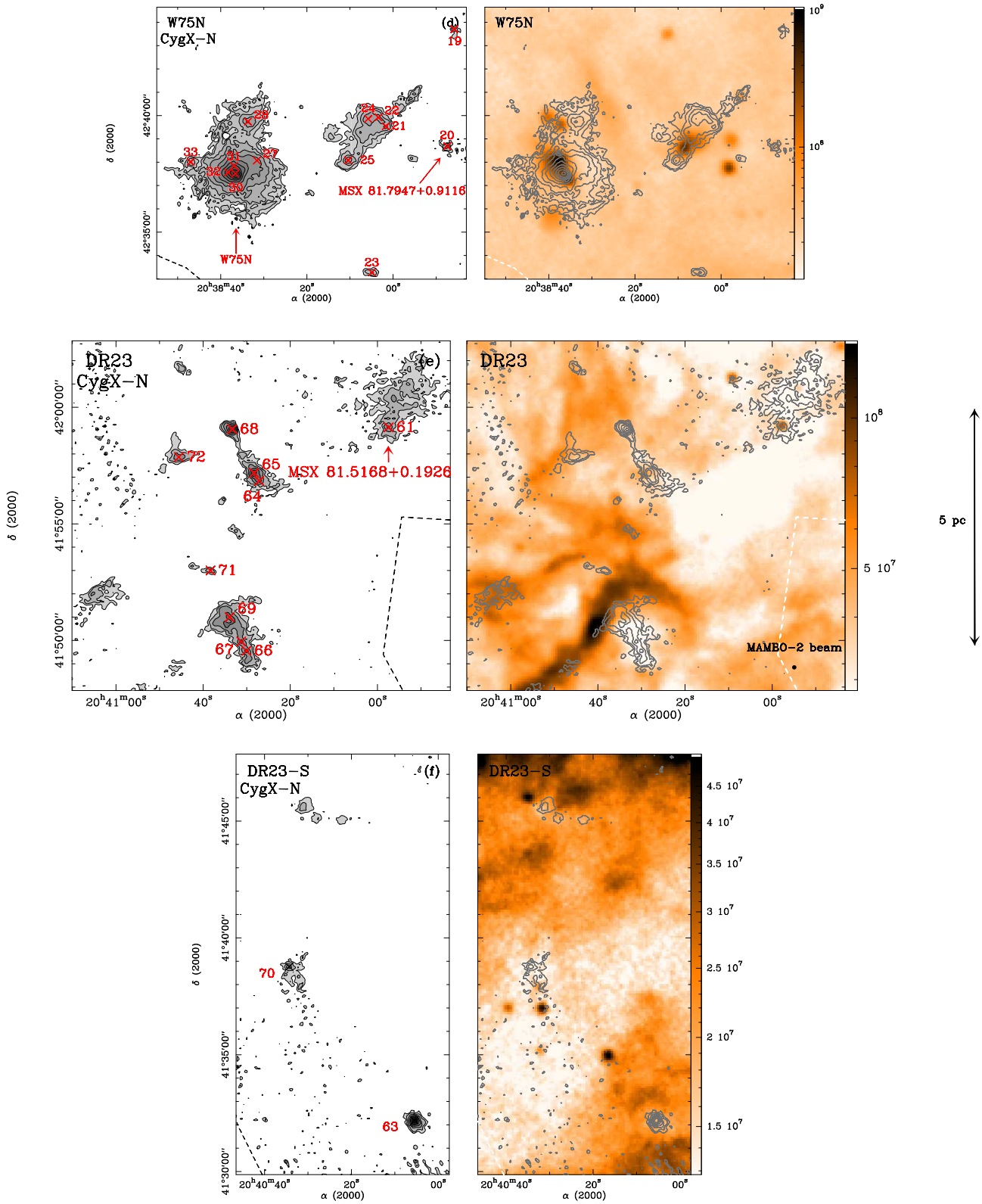

Fig. 12. (continued) Same caption for the region around W75N (**d**) and DR23 (**e**), and south of DR23 (**f**). Contour levels are logarithmic and go from 40 to 4 800 mJy beam^{-1} in **d**, and from 40 to 800 mJy beam^{-1} in **e** and **f**.

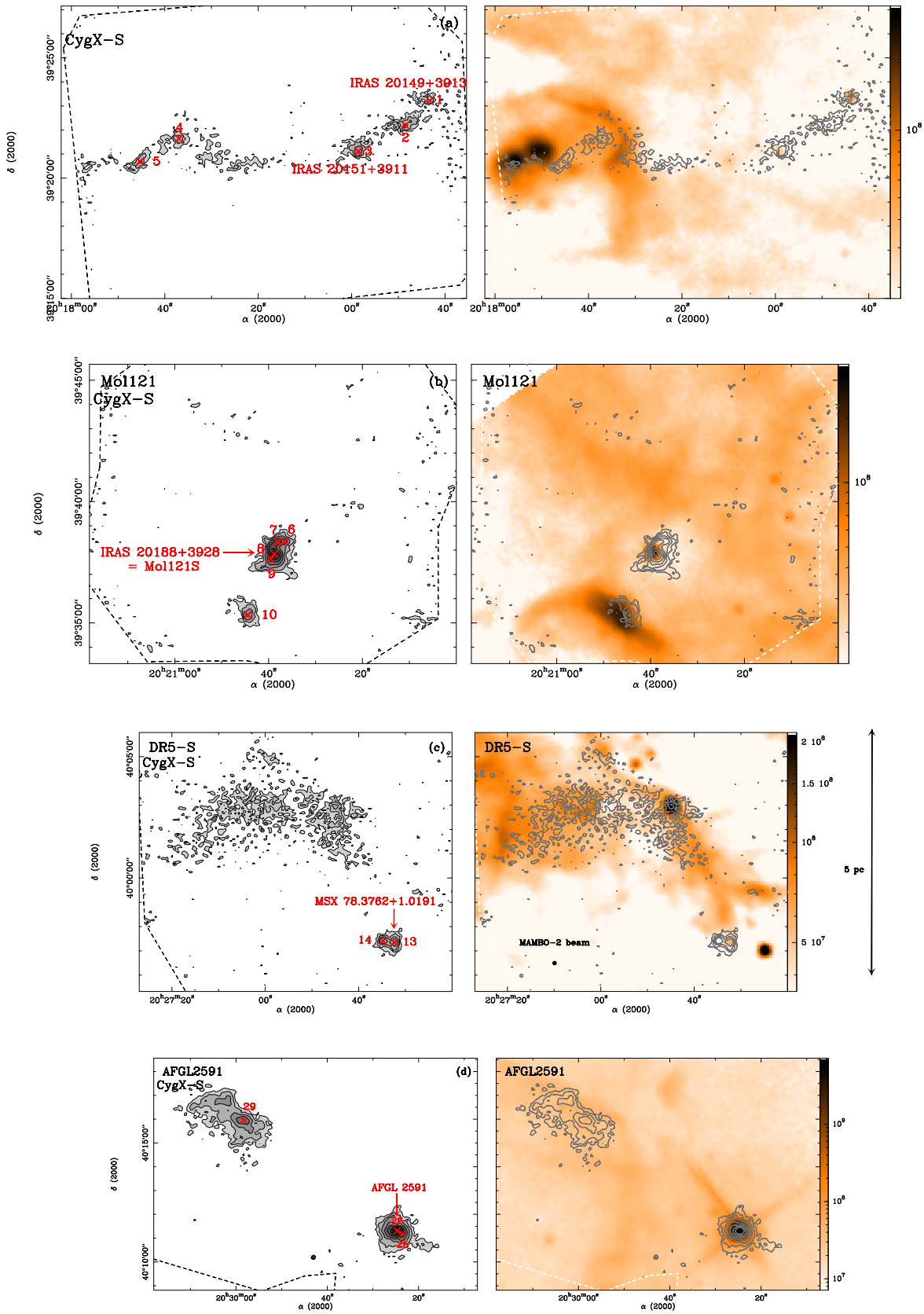

Fig. 13. Same convention as Fig. 12 for MAMBO maps of CygX-South extracted from Fig. 2b. Regions shown are the most western part of CygX-South (**a**), around Mol121 (**b**), around AFGL 2591 (**c**), and south of DR5 (**d**). Contour levels are logarithmic and go from 60 to 180 mJy beam^{-1} in **a**, from 60 to 2 000 mJy beam^{-1} in **b**, from 40 to 200 mJy beam^{-1} in **c**, and from 40 to 1 000 mJy beam^{-1} in **d**.

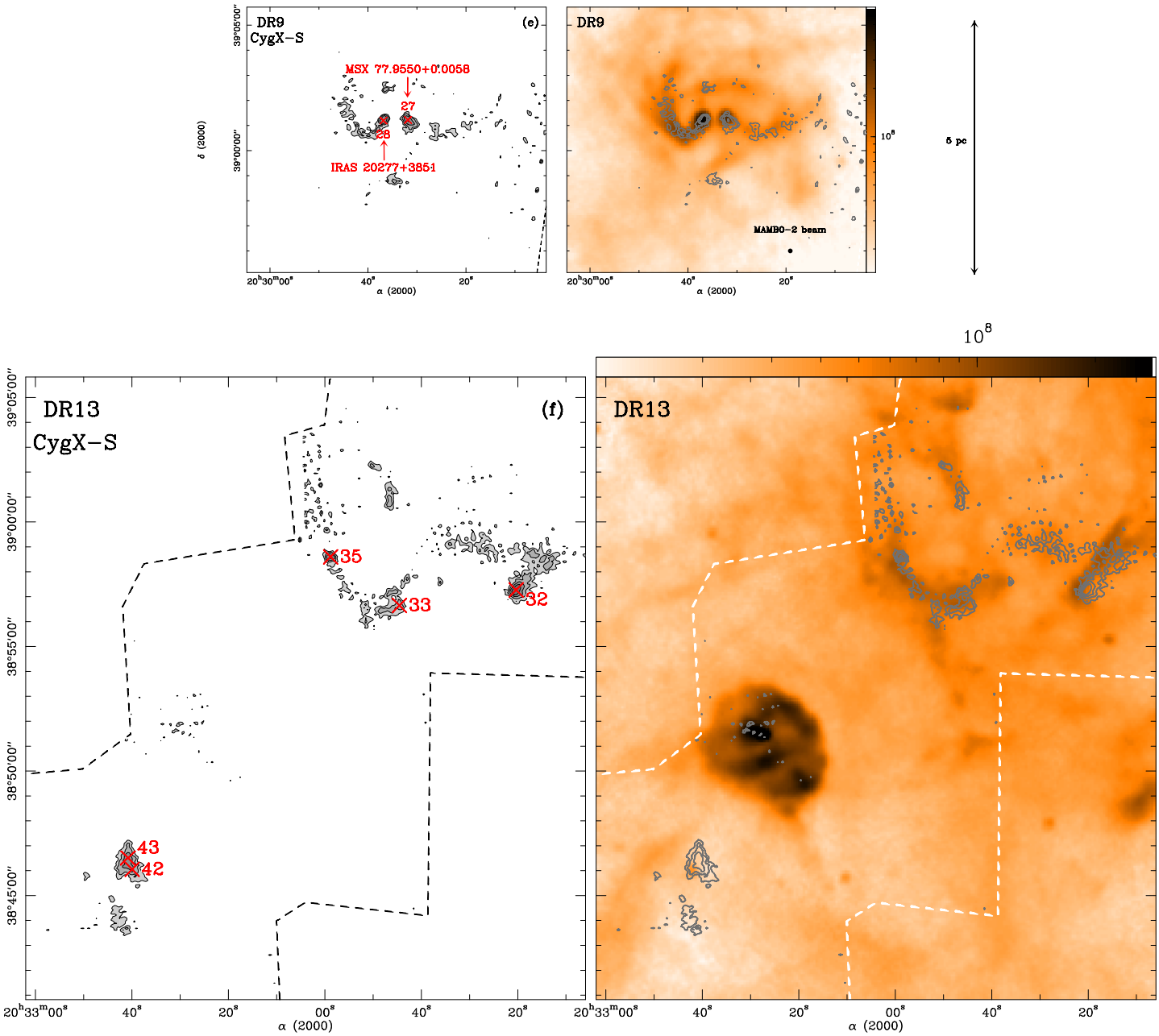

Fig. 13. (continued) Same caption for the region around DR9 (**e**) and DR13 (**f**). Contour levels are logarithmic and go from 40 to 200 mJy beam^{-1} in **e**, and from 60 to 300 mJy beam^{-1} in **f**.

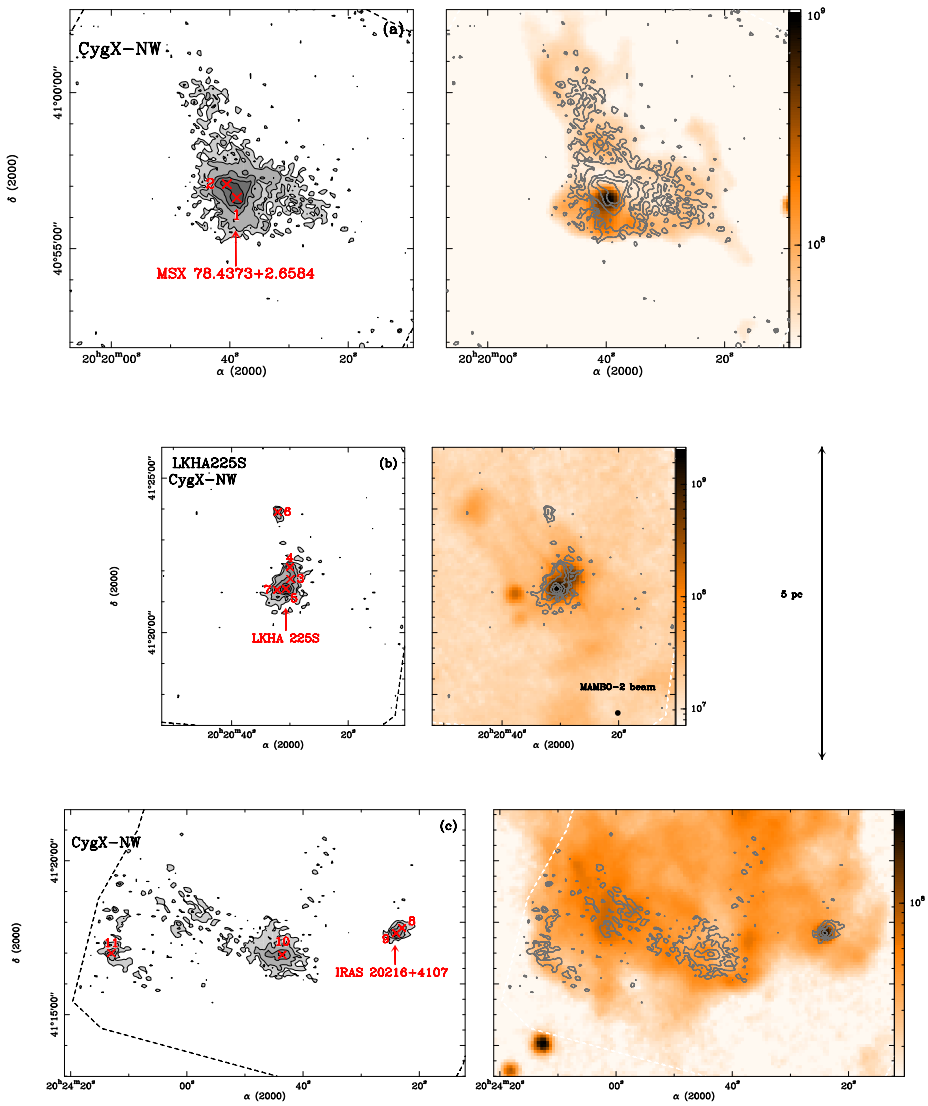

Fig. 14. Same convention as Fig. 12 for MAMBO maps of CygX-NW extracted from Fig. 2c. Regions shown are those of Fig. 2c4 (**a**), of Fig. 2c3 (**b**), and of Fig. 2c2 (**c**). Contour levels are logarithmic and go from 40 to 300 mJy beam^{-1} in **a**, from 60 to 400 mJy beam^{-1} in **b**, and from 60 to 250 mJy beam^{-1} in **c**.

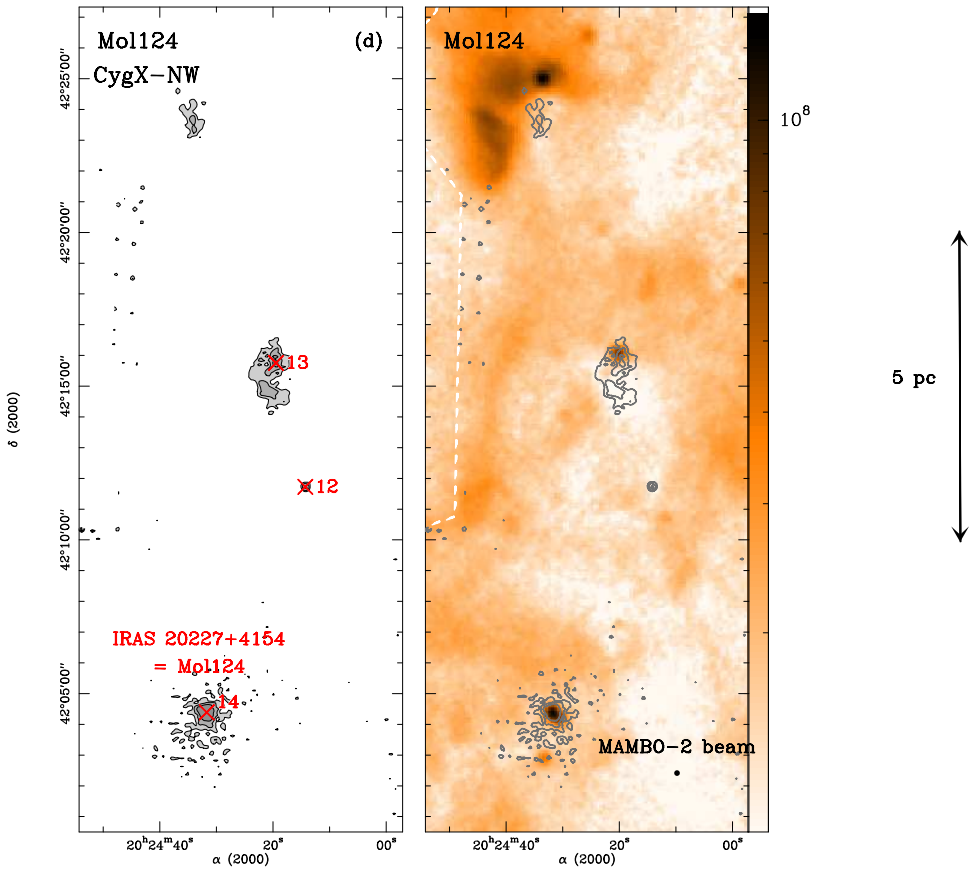

Fig. 14. (continued) Same caption for the region around Mol124 (**d**). Contour levels are logarithmic and go from 60 to 180 mJy beam^{-1} in **d**.

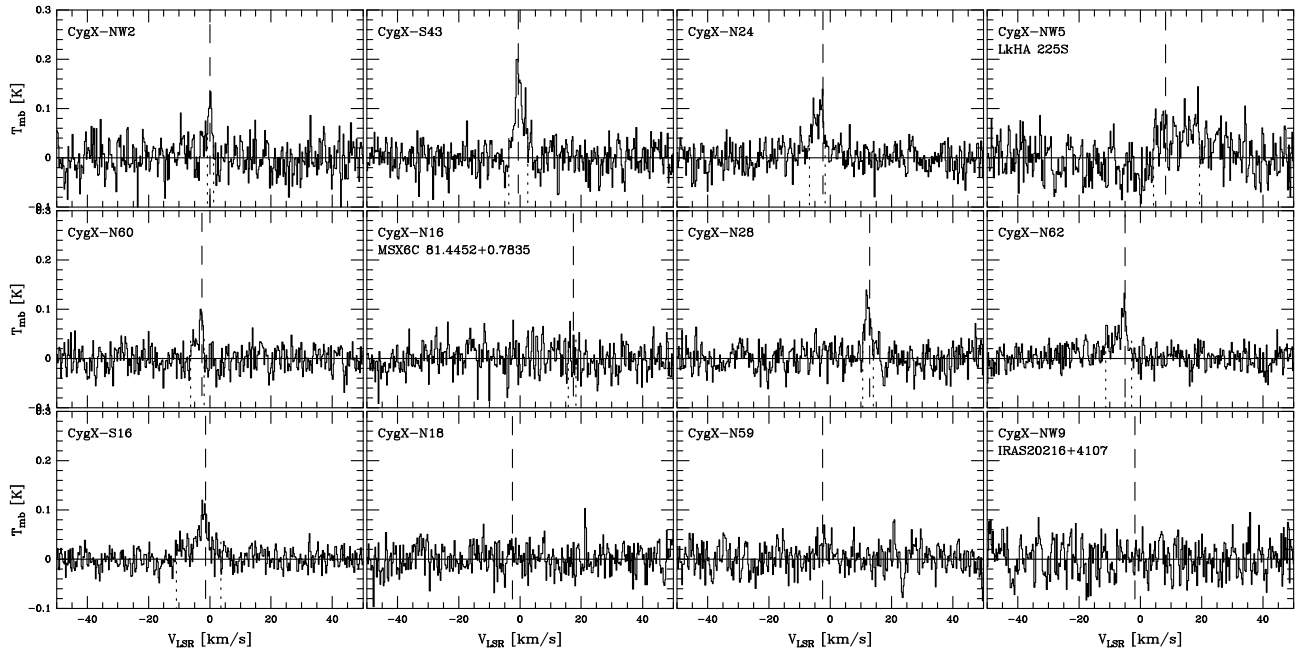

Fig. 15. SiO(2 − 1) emission toward 12 additional fragments, ordered by decreasing $M_{1.2\mathrm{mm}}$.